Computer Physics Communications 258 (2021) 107579

Contents lists available at ScienceDirect

Computer Physics Communications

journal homepage: www.elsevier.com/locate/cpc

Quantum turbulence simulations using the Gross–Pitaevskii equation: High-performance computing and new numerical benchmarks ☆

Michikazu Kobayashi [a], Philippe Parnaudeau [b], Francky Luddens [c], Corentin Lothodé [c], Luminita Danaila [d], Marc Brachet [e], Ionut Danaila [c,*]

[a] School of Environmental Science and Engineering, Kochi University of Technology, Japan
[b] Institut Pprime, CNRS, Université de Poitiers - ISAE-ENSMA - UPR 3346, 11 Boulevard Marie et Pierre Curie, 86962 Futuroscope Chasseneuil Cedex, France
[c] Université de Rouen Normandie, Laboratoire de Mathématiques Raphaël Salem, CNRS UMR 6085, Avenue de l'Université, BP 12, F-76801 Saint-Étienne-du-Rouvray, France
[d] Université de Rouen Normandie, CORIA, CNRS UMR 6614, Avenue de l'Université, BP 12, F-76801 Saint-Étienne-du-Rouvray, France
[e] Laboratoire de Physique de l'École Normale Supérieure, ENS, Université PSL, CNRS, Sorbonne Université, Université de Paris, F-75005 Paris, France

ARTICLE INFO

Article history:
Received 7 March 2020
Received in revised form 21 August 2020
Accepted 26 August 2020
Available online 29 August 2020

Keywords:
Quantum Turbulence
Gross–Pitaevskii equation
Taylor–Green
ABC
Parallel computing
Spectral method

ABSTRACT

We present high-performance and high-accuracy numerical simulations of quantum turbulence modelled by the Gross–Pitaevskii equation for the time-evolution of the macroscopic wave function of the system. The hydrodynamic analogue of this model is a flow in which the viscosity is absent and all rotational flow is carried by quantized vortices with identical topological line-structure and circulation. Numerical simulations start from an initial state containing a large number of quantized vortices and follow the chaotic vortex interactions leading to a vortex-tangle turbulent state. The Gross–Pitaevskii equation is solved using a parallel (MPI-OpenMP) code based on a pseudo-spectral spatial discretization and second order splitting for the time integration. We define four quantum-turbulence simulation cases based on different methods used to generate initial states: the first two are based on the hydrodynamic analogy with classical Taylor–Green and Arnold–Beltrami–Childress vortex flows, while the other two methods use a direct manipulation of the wave function by generating a smoothed random phase field, or seeding random vortex-ring pairs. The dynamics of the turbulent field corresponding to each case is analysed in detail by presenting statistical properties (spectra and structure functions) of main quantities of interest (energy, helicity, etc.). Some general features of quantum turbulence are identified, despite the variety of initial states. Numerical and physical parameters of each case are presented in detail by defining corresponding benchmarks that could be used to validate or calibrate new Gross–Pitaevskii codes. The efficiency of the parallel computation for a reference case is also reported.

1. Introduction

The study of quantum fluids, realized in superfluid helium and atomic Bose–Einstein condensates (BEC), has become a central topic in various fields of physics, such as low temperature physics, fluid dynamics of inviscid flows, quantum physics, statistical physics, cosmology, etc. One of the striking features of quantum fluids is the nucleation of vortices with quantized (fixed) circulation, when an external forcing is applied (rotation, stirring, etc.). The observation of quantized vortices, as a signature of the superfluid (zero-viscosity) nature of these flow systems, was extensively explored in different experimental settings of superfluid helium or BEC. Configurations with a large number of quantized vortices tangled in space can evolve to Quantum Turbulence (QT), generally referred to as *vortex tangle turbulence*. While QT in superfluid helium has been largely studied in the last two decades (see dedicated volumes [1–4]), only recent experimental and theoretical studies [5–8] reported different possible routes to QT in BEC.

☆ The review of this paper was arranged by Prof. Hazel Andrew.

* Corresponding author.
E-mail addresses: kobayashi.michikazu@kochi-tech.ac.jp (M. Kobayashi), philippe.parnaudeau@univ-poitiers.fr (P. Parnaudeau), francky.luddens@univ-rouen.fr (F. Luddens), corentin.lothode@univ-rouen.fr (C. Lothodé), luminita.danaila@coria.fr (L. Danaila), marc-etienne.brachet@lps.ens.fr (M. Brachet), ionut.danaila@univ-rouen.fr (I. Danaila).

https://doi.org/10.1016/j.cpc.2020.107579
0010-4655/

A promising path of research in exploring QT is based on the analogy with classical turbulence (CT), observed in conventional viscous fluids and governed by the Navier–Stokes equations. Classical turbulent flows are characterized by the chaotic motion of vortical eddies that populate a continuous hierarchy of intensities and scales, from the large (integral) scale of the flow, down to the Kolmogorov's viscous length scale. The classical turbulent cascade of energy between scales is characterized by the Kolmogorov's power-law spectrum [9] in the regime of vanishing viscosity (*i.e.* large to infinite Reynolds numbers). Quantum turbulence appears then as an equivalent regime, since superfluids are assimilated to flows with zero viscosity. Both finite- and zero-viscosity regimes can be experimentally obtained in liquid helium by changing the temperature: above the lambda transition temperature (2.17 K) the liquid is normal (viscous) and well below it is a pure superfluid. Experimental measurements in superfluid helium-4 at temperatures below 2 K [10] provided indeed evidence of Kolmogorov's law for the kinetic energy cascade. However, vortex interaction mechanisms are different in the two types of turbulence. Unlike classical vortex eddies, vortices in QT are identical topological line defects in the fluid density field and their circulation is quantized (in units of Planck's constant over the atomic mass). In QT, bundles of quantum line vortices play the role of classical vortex eddies. Since visualizations in QT experiments are not yet enough precise to provide an accurate image of vortex interactions, numerical simulations are then needed. The vortex filament (VF) and the Gross–Pitaevskii (GP) models are used in the literature to numerically explore vortex interactions mechanisms in QT. The VF model represents quantized vortices as infinitely thin lines and follows their evolution by integrating the Biot–Savart–Laplace law over the vortex filament tangle. This model proved very useful in studying superfluid helium-4 [11]. The GP model is the simplest mathematical model for a superfluid at zero-temperature and it will be the focus of this paper. It can be also regarded as a theoretical and numerical framework used to investigate the inviscid limit of a fully-developed CT. For a comprehensive description of different models of QT, see recent reviews by Halperin and Tsubota [4], Brachet [12], Barenghi et al. [13] and Tsubota et al. [11].

The Gross–Pitaevskii equation (GPE) is a nonlinear Schrödinger equation with cubic nonlinearity. It describes, in the theoretical limit of absolute zero temperature, the time evolution of the macroscopic complex wave function ψ (identical for all particles) defining a weakly interacting Bose system. Consequently, the GP model naturally applies to numerical studies of QT in Bose–Einstein condensates [14]. The relevance of the GPE for describing QT in superfluid helium is discussed in Section 3.3. For general QT flows, the GP model offers the advantage that quantized vortices appear naturally as topological line defects, resulting from the $U(1)$ symmetry breaking of the phase shift of ψ. Subsequent vortex phenomena (reconnection, annihilation) are intrinsically described by the model. Supplementary phenomenological models are needed in the VF approach to take into account the same vortex mechanisms. As a consequence, QT simulations based on the GPE (denoted hereafter as GPE-QT) were largely used in the literature to study vortex interactions and statistical properties of QT in the zero-temperature limit.

There are several challenges when setting a numerical simulation to investigate GPE-QT: *(i)* generate a physically and mathematically sound initial state with many quantized vortices that finally evolve to a statistically steady state of QT, *(ii)* use accurate numerical methods that preserve the invariants of the GPE when long time-integration is necessary, *(iii)* design numerical codes affording large grid resolutions, necessary to accurately capture the dynamics of vortices and *(iv)* compute appropriate (statistical) diagnostic tools to analyse the superfluid flow evolution.

We use in this contribution a modern parallel (MPI-OpenMP) numerical code satisfying the requirements *(ii)* and *(iii)*. The code is called GPS (Gross–Pitaevskii Simulator) [15] and is based on a Fourier-spectral space discretization and up-to-date numerical methods: a semi-implicit backward-Euler scheme with Krylov preconditioning for the stationary GP equation [16] and various schemes (Strang splitting, relaxation, Crank–Nicolson) for the real-time GP equation [17]. The GPS code offers a solid framework to address in detail challenges *(i)* and *(iv)*, for which we review previous models and bring new contributions.

A great deal of attention has been lately devoted to the development of accurate numerical schemes to solve different forms of the GPE, from the classical (stationary or time-dependent) GPE, to systems of coupled GPEs and more recent formulations (*e.g.* with non-local or high-order interactions). For recent reviews of numerical methods for GPE, see [17–21]. Several software packages for solving the GPE were deposited in the CPC Program Library. The spatial discretization is generally based on spectral [16,22–24], finite-elements [25,26] or finite-difference [27–32] methods. Provided programs are written in Fortran [22,27], C [28,29], Matlab [16,23,24, 29,31], FreeFem++ [26] or C and Fortran with OpenMP [32]. None of these programs deal with QT simulations, but can eventually be extended to perform such simulations using the procedures explained in this paper.

As in classical turbulence, the numerical and physical accuracy of the initial condition is crucial in computing properties of numerically generated QT. Using the hydrodynamic analogy for the GP model (through the Madelung transform, as explained below), pioneering numerical simulations of GP-QT [33–35] suggested initial conditions and statistical analysis tools inspired from CT. A velocity field, derived from the well-known classical flow with Taylor–Green (TG) vortices, was imposed to the superfluid flow. An initial wave function, with nodal lines corresponding to vortex lines of the velocity, was thus generated. This initial wave function was then used in the Advective Real Ginzburg–Landau equation (ARGLE), equivalent to the imaginary-time GP equation with Galilean transformation (see also below), to reduce the acoustic emission of the initial field. The result of the ARGLE procedure was finally used as initial field for the time-dependent GP simulation. A similar approach was more recently used by replacing the TG vortices with the Arnold–Beltrami–Childress (ABC) classical vortex flow [36,37]. If this approach is well suited to control the hydrodynamic characteristics of the initial superfluid flow (Mach number, helicity), it involves supplemental technicalities and computations through the ARGLE procedure. We suggest in this paper two new approaches to generate the initial condition for the GP-QT simulations, based on the direct manipulation of the wave function. The ARGLE procedure is thus avoided. The first method prescribes a smoothed random-phase (SRP) for the wave function, while the second one generates random vortex rings (RVR). The two new methods, which are simple to implement, are shown to develop QT fields with similar statistical properties as those obtained using the TG or ABC classical initial conditions. Nevertheless, the dynamics of the superfluid flow is different. Compared to TG and ABC cases, in the SRP case the initial field is vortex free and dominated by the compressible kinetic energy; vortices nucleate progressively and do not display long vortex lines. For the RVR flow, evolution is opposite to that observed for the SRP case: in the early stages of the time evolution the incompressible kinetic energy is dominant; the compressible kinetic energy then starts to increase due to sound emissions through vortex reconnections. However, like in well-documented TG and ABC cases, a Kolmogorov-like scaling of the incompressible kinetic energy spectrum is obtained for the new SRP and RVR cases.

Concerning the analysis of the QT field, we present classical diagnostic tools (inspired from CT), as the energy decomposition and associated spectra [33,34] and also new ones, as the second-order structure function, not reported in the previously cited studies. This

supplements the statistical description of the superfluid flow. We also carefully investigate the influence of numerical parameters (as the grid resolution of a vortex, the maximum resolved wave-number and the computed local Mach number) on the characteristic of QT. This topic is generally very briefly addressed in physical papers on GP-QT.

Starting from the observation that in previously published studies of GP-QT, the focus was mainly given to the physics of turbulence, this paper is also intended to define in detail numerical benchmarks in the framework of parallel computing. We start by revisiting classical GP-QT settings (based on TG and ABC flows). New results obtained with our high-performance/high-accuracy parallel code are compared with available data in the literature. We then present the new numerical benchmarks, based on random phase fields or random vortex rings generation. The new benchmarks offer a new perspective in comparing the classical CT based approaches to more GP-oriented models. For all benchmarks, we offer a comprehensive description of the numerical and physical parameters and give checkpoint values for validating each step of the simulation. This could be useful to assess new numerical methodologies or tune/validate new modern GP numerical codes.

The organization of the paper is as follows. Section 2 introduces the GP mean field equation, its stationary version and the hydrodynamic analogy. Section 3 presents the mathematical and physical QT model used in the present numerical simulations. The main characteristics of the quantum flow (healing length, sound velocity) and the notion of quantized vortex are introduced. The Bogoliubov dispersion relation and the validity of the model are also discussed. In Section 4 we present the main diagnostic quantities generally used to analyse a QT flow: spectra of compressible and incompressible kinetic energies, velocity structure functions and helicity. The numerical methods used to solve the GP equation and the associated GPS code are described in Section 5. An extended subsection is devoted to the derivation of dimensionless equations. The particular numerical methods used in this study to advance the GP wave function in imaginary-time (ARGLE) or real-time (GP) are also described. Section 6 presents in detail four different approaches to generate the initial field for the simulation of decaying GP-QT: Taylor–Green (TG), Arnold–Beltrami–Childress (ABC), smoothed random phase (SRP) and random vortex rings (RVR). Each method is associated to a benchmark. The results obtained for the four benchmarks are discussed in Section 7. We present values, spectra and structure functions of main quantities of interest (energy, helicity, etc.) that could be useful to benchmark numerical codes simulating QT with the GP model. Finally, the main features of the benchmarks and their possible extensions are summarized in Section 8. Appendix presents strong scalability tests of the computation code used to run a specific case (the ABC flow) in both MPI and hybrid MPI-OpenMP configurations.

2. The Gross–Pitaevskii model

In the zero-temperature limit, the superfluid system of weakly interacting bosons of mass m, is described by the Gross–Pitaevskii mean field equation [38]:

$$i\hbar\frac{\partial}{\partial t}\psi(\mathbf{x},t)=\left(-\frac{\hbar^2}{2m}\nabla^2+V_{\text{trap}}(\mathbf{x})+g\,|\psi(\mathbf{x},t)|^2\right)\psi(\mathbf{x},t), \tag{1}$$

where V_{trap} is the external trapping potential and g the non-linear interaction coefficient

$$g=\frac{4\pi\hbar^2 a_s}{m}, \tag{2}$$

with a_s the s-wave scattering length for the binary collisions within the system.

The complex wave function ψ is generally represented as (Madelung transform):

$$\psi=\sqrt{n(\mathbf{x},t)}\,e^{i\theta(\mathbf{x},t)},\quad n(\mathbf{x},t)=|\psi(\mathbf{x},t)|^2=\psi(\mathbf{x},t)\psi^*(\mathbf{x},t), \tag{3}$$

with n the atomic density and θ the phase of the order parameter. We denote by ψ^* the complex conjugate of the wave function.

The main integral quantities conserved by the GPE (1) are the number of atoms N

$$N=\int|\psi|^2\,d\mathbf{x}=\int n\,d\mathbf{x}. \tag{4}$$

and the energy of the system

$$E(\psi)=\int\left(\frac{\hbar^2}{2m}|\nabla\psi|^2+V_{\text{trap}}\,|\psi|^2+\frac{1}{2}g|\psi|^4\right)d\mathbf{x}. \tag{5}$$

Stationary solutions to the GPE are obtained by considering that the wave function evolves in time as:

$$\psi(\mathbf{x},t)=\Psi(\mathbf{x})\exp(-i\mu t/\hbar), \tag{6}$$

with μ the chemical potential. Note that $|\psi|=|\Psi|$ and the number of atoms in (4) is conserved by the stationary field. The time-evolution GP equation (1) then reduces to the stationary (time-independent) GP equation:

$$-\frac{\hbar^2}{2m}\nabla^2\Psi+V_{\text{trap}}\Psi+g|\Psi|^2\Psi=\mu\Psi. \tag{7}$$

The chemical potential μ is fixed by the normalization condition (4) and expressed from (6) and (7) as:

$$\begin{aligned}\mu&=\frac{1}{N}\int\left(\frac{\hbar^2}{2m}|\nabla\Psi|^2+V_{\text{trap}}\,|\Psi|^2+g|\Psi|^4\right)d\mathbf{x}\\&=\frac{1}{N}\left(E(\Psi)+\int\frac{1}{2}g|\Psi|^4\,d\mathbf{x}\right).\end{aligned} \tag{8}$$

The hydrodynamic analogy of the GPE (1) is obtained by relating the wave function ψ to a superfluid flow of mass density

$$\rho(\mathbf{x}, t) = m\, n(\mathbf{x}, t) = m\, |\psi(\mathbf{x}, t)|^2, \tag{9}$$

and velocity

$$\mathbf{v}(\mathbf{x}, t) = \frac{\hbar}{m} \nabla\theta(\mathbf{x}, t) = \frac{\hbar}{\rho} \frac{\psi^* \nabla\psi - \psi \nabla\psi^*}{2i}. \tag{10}$$

For a flow of non-vanishing density ($\rho \neq 0$), we infer from (10) that the superfluid is irrotational:

$$\nabla \times \mathbf{v} = 0. \tag{11}$$

The evolution equations for the density ρ and the velocity $\mathbf{v}$ can be derived by inserting the Madelung transform (3) in the GPE (1), separating the imaginary and real parts, and using definitions (9)–(10):

$$\frac{\partial \rho}{\partial t} + \nabla \cdot (\rho \mathbf{v}) = 0, \tag{12}$$

$$\frac{\partial \mathbf{v}}{\partial t} + \frac{1}{2}\nabla(\mathbf{v}^2) = -\frac{1}{m}\nabla\left(gn + V_{\text{trap}}\right) + \frac{\hbar^2}{2m^2}\nabla\left(\frac{1}{\sqrt{\rho}}\nabla^2(\sqrt{\rho})\right). \tag{13}$$

Eq. (12) is the continuity equation of the superflow, expressing the conservation of the number of particles N given by (4). Eq. (13) is the momentum equation and its last term in the right-hand side is the gradient of the so-called *quantum pressure*. This term is a direct consequence of the Heisenberg uncertainty principle [38] and depends on the gradient of density, suggesting that quantum effects are important in non-uniform gases and, for uniform systems, close to vortex cores. The system of Eqs. (12)–(13) is equivalent to the original GPE (1).

3. Mathematical and physical model for quantum turbulence

The mathematical and physical model used in this study is based on the GPE (1) in which the trapping potential is set to zero ($V_{\text{trap}} = 0$). The main consequence of this assumption is that the momentum equation (13) reduces, after neglecting the quantum pressure term, to:

$$\frac{\partial \mathbf{v}}{\partial t} + (\mathbf{v} \cdot \nabla)\mathbf{v} = -\frac{1}{\rho}\nabla\left(\frac{g\rho^2}{2m^2}\right). \tag{14}$$

Eqs. (12) and (14) are now similar to the Euler equations describing the evolution of a compressible, barotropic and inviscid classical flow with pressure:

$$P = \frac{g\rho^2}{2m^2}. \tag{15}$$

We thus obtain a GPE-based model that is analogous to that describing a classical flow of a fluid with zero viscosity. Note that Eqs. (12) and (14) show that the total momentum of the superfluid,

$$\mathbf{p} = \int (\rho \mathbf{v})\, d\mathbf{x} = \hbar \int \mathcal{I}mag(\psi^* \nabla\psi)\, d\mathbf{x}, \tag{16}$$

is conserved. This is not generally the case if $V_{\text{trap}} \neq 0$. To summarize, the three main integral invariants of the model are: the number of particles N (4), the energy E (5) and the momentum $\mathbf{p}$ (16).

The idea behind the model used in this study is to represent the quantum turbulent flow as an infinite background uniform flow of constant density to which many vortices are superimposed in the initial state. The dynamics of this initial state is then followed by numerically solving the GPE (1). Vortices interact to generate a vortex-tangle turbulent state that finally reach a statistical convergent state. This approach is similar to that used in classical fluids to simulate decaying turbulence. Note that, in contrast to CT Navier–Stokes based models, there is no dissipation in the present zero-temperature GP model. Phenomenological models for dissipation in superfluids could be added in the GPE to model thermal excitations [39].

3.1. Uniform background flow

A second consequence of the assumption $V_{\text{trap}} = 0$ is that the stationary GPE (7) admits an elementary solution Ψ_0 representing a flow with constant density $\rho = \rho_0$. From (6) and (7), we infer that:

$$\mu_0 = g|\Psi_0|^2 = g|\psi_0|^2 = gn_0 = g\,\frac{\rho_0}{m}. \tag{17}$$

The solution Ψ_0 could be taken as real and represents a first approximation of a quantum uniform flow developing in a container of volume V, far from the walls. This flow is compressible, with pressure given by Eq. (15) and sound velocity c defined as in classical hydrodynamics:

$$c = \sqrt{\frac{\partial P_0}{\partial \rho_0}} = \frac{\sqrt{g\rho_0}}{m} = \sqrt{\frac{gn_0}{m}}. \tag{18}$$

The sound velocity gives a characteristic velocity of the uniform flow. To have a complete space–time description of the system we need to introduce a characteristic length scale. The healing length indicates the distance over which density variations take place in the

system. The following expression for the healing length is obtained from the momentum equation (13) by imposing that the pressure term balances the quantum pressure term over the healing length:

$$\xi = \frac{\hbar}{\sqrt{2mgn_0}} = \frac{\hbar}{\sqrt{2m\mu_0}} = \frac{1}{\sqrt{2}}\frac{\hbar}{mc}. \tag{19}$$

It follows that the quantum pressure is negligible for distances $R \gg \xi$, which is exactly the domain of validity of the hydrodynamic analogy with the Euler equations.

3.2. Quantized vortices

The definition (10) of the superflow velocity becomes singular along lines with vanishing density ($\rho = 0$). The lines along which both real and imaginary part the order parameter are zero define topological defects, known as *quantum vortices*. The hydrodynamic analogy through the Madelung transform becomes singular when vortices are present in the superflow. A detailed review of mathematical problems related to the Madelung transform in presence of quantum vortices is offered in [40]. It is important to recall that vortex solutions are not singular solutions of the GPE (1).

A straight-line vortex in a uniform flow could be represented using cylindrical coordinates (r, φ, z) as [38]:

$$\Psi_v = \sqrt{n_0} f(\eta) e^{i\kappa\varphi}, \tag{20}$$

where $\eta = r/\xi$ and κ is necessarily an integer to ensure that the wave function is single valued. Using (10) we infer that the velocity around the vortex line is tangential and singular for $r = 0$:

$$\mathbf{v}_v = \frac{\hbar}{m}\frac{1}{r}\frac{\partial(\kappa\varphi)}{\partial\varphi}\mathbf{e}_\varphi = \frac{\hbar}{m}\frac{\kappa}{r}\mathbf{e}_\varphi. \tag{21}$$

The circulation around a regular path $\mathcal{C}$ surrounding this vortex line is then:

$$\Gamma_v = \oint_{\mathcal{C}} \mathbf{v}_v \cdot d\mathbf{l} = (2\pi)\kappa\frac{\hbar}{m} = \kappa\frac{h}{m}. \tag{22}$$

This quantification of the vortex line circulation is the outstanding difference between quantum and classical hydrodynamics. The integer κ is usually referred to as winding number or charge of the vortex. The asymptotic behaviour of the vortex solution (20) near the origin ($r = 0$) is well-known [41]:

$$f(\eta) \sim \eta^{|\kappa|} + \mathcal{O}(\eta^{|\kappa|+2}), \quad \eta \to 0, \tag{23}$$

suggesting that the vortex core, *i.e.* the region near the vortex line where the density is varying in a significant way, is of the order of the healing length ξ.

Using (21), the kinetic energy ($\int \rho\mathbf{v}_v^2 d\mathbf{x}$) of the vortex solution results to be proportional to κ^2 [*e.g.* 42]. This implies that a multiply quantized vortex with $\kappa > 1$ is energetically unstable and split into κ-singly quantized vortices in the GP model.

3.3. Dispersion relation and validity of the model

Since the GPE (1) sustains wave solutions, it is interesting to estimate the response of the system to small perturbations. The Bogoliubov–de Gennes model is based on the linearization of (1) around a stationary solution Ψ_0 by assuming a perturbation of small amplitude of the form:

$$\delta\psi = a(\mathbf{x})e^{-i\omega t} + b^*(\mathbf{x})e^{i\omega^* t}, \tag{24}$$

where a, b are complex functions (of small amplitudes) and ω is a complex frequency. In the case of the uniform flow, $\Psi_0 = \sqrt{n_0}$ and perturbations are taken as plane waves $a(\mathbf{x}) = ue^{i\mathbf{k}\cdot\mathbf{x}}$, $b(\mathbf{x}) = ve^{i\mathbf{k}\cdot\mathbf{x}}$, with $\mathbf{k}$ the wave number vector. We obtain that the resulting Bogoliubov–de Gennes system admits non-trivial solution if

$$(\hbar\omega)^2 = \left(\frac{\hbar^2}{2m}\mathbf{k}^2\right)^2 + (gn_0)\frac{\hbar^2}{m}\mathbf{k}^2. \tag{25}$$

Using (18) to express the sound velocity and (19) for the healing length, the Bogoliubov dispersion relation (25) becomes:

$$\omega = ck\sqrt{1 + \frac{\xi^2k^2}{2}}. \tag{26}$$

This dispersion relation is linear for ($k\xi \ll 1$) and the excitations in this regime are called *phonons* (sound waves). Going back to the momentum equation (13), we can easily see that in the phonons regime, the quantum pressure is negligible in front of the hydrodynamic pressure. Consequently, the validity of the hydrodynamic analogy is limited to the phonons excitations, a regime where the quantum pressure could be neglected. In helium II, due to strong interactions between particles, the dispersion relation has a different shape, with a linear regime followed by a quadratic regime with a maxon (local maximum) and a roton (local minimum) [42]. The excitations in the quadratic region near the minimum of the dispersion curve are called rotons. Consequently, using the GPE allows us to capture only the phonons regime of excitations in a quantum flow.

A second drawback of the GP model in describing superfluid helium turbulence comes from compressibility effects. An important feature in the hydrodynamic description of superfluid helium is that the fluid is almost incompressible in both its normal (viscous) and superfluid components. On the other hand, the hydrodynamic description (12)–(14) of the GPE shows the compressibility of the GP fluid. We expect, however, that the GP model applied for low Mach number flows (*i.e.* the mean superfluid velocity is much smaller than

the sound velocity) provides a good qualitative representation of the superfluid helium flow and, in particular, of vortex interactions. From a physical point of view, both drawbacks (dispersion relation and compressibility) of the GPE model can be alleviated by adding non-local or higher-order non-linear terms. This idea was suggested by Berloff et al. [43] who added to the GPE a non-local potential and non-linear terms up to order 7 (instead of 3 for the standard GPE) to modify the equation of continuity and model more realistic dispersion curves.

4. Description of the quantum turbulent flow

4.1. Energy decomposition

The energy is the first integral quantity that will be used to characterize the QT flow field. The accuracy of numerical simulations in conserving this quantity is an important checkpoint to validate the numerical scheme and the grid resolution. As in CT, energy spectra will be used to identify different (Kolmogorov) regimes/ranges in the structure of the turbulent field. Starting from the observation that the QT field can be viewed as a background uniform flow to which a large number of quantum vortices are superimposed, the total energy of the system in QT studies [*e.g.* 34,44] is generally computed using the form:

$$E_T(\psi) = \int \left(\frac{\hbar^2}{2m} |\nabla \psi|^2 + \frac{1}{2} g \left(|\psi|^2 - |\Psi_0|^2 \right)^2 \right) d\mathbf{x}, \tag{27}$$

where $|\Psi_0|^2 = n_0$ is the atomic density of the uniform flow. This expression is strictly equivalent to the form (5) of the energy because of the conservation of the number of atoms (4). The corresponding GP equation, equivalent to (1) is then:

$$i\hbar \frac{\partial}{\partial t} \psi(\mathbf{x}, t) = \left(-\frac{\hbar^2}{2m} \nabla^2 + g \left(|\psi(\mathbf{x}, t)|^2 - |\Psi_0|^2 \right) \right) \psi(\mathbf{x}, t), \tag{28}$$

Using the hydrodynamic analogy presented in Section 2, the total energy (27) can be also presented as:

$$E_T(\rho, \mathbf{v}) = \int \left(\frac{1}{2} \rho \mathbf{v}^2 + \frac{\hbar^2}{2m^2} |\nabla \sqrt{\rho}|^2 + \frac{1}{2m^2} g \left(\rho - \rho_0 \right)^2 \right) d\mathbf{x}. \tag{29}$$

The three terms in (29) correspond to [34,44]:
– the kinetic energy

$$E_{\text{kin}} = \int \frac{|\sqrt{\rho}\mathbf{v}|^2}{2} d\mathbf{x}, \tag{30}$$

– the so-called quantum energy (expressed using (19))

$$E_{\text{q}} = \int \frac{\hbar^2}{2m^2} |\nabla \sqrt{\rho}|^2 d\mathbf{x} = \int c^2 \xi^2 |\nabla \sqrt{\rho}|^2 d\mathbf{x}. \tag{31}$$

– and the internal energy (expressed using (18)):

$$E_{\text{int}} = \int \frac{1}{2m^2} g \left(\rho - \rho_0 \right)^2 d\mathbf{x} = \int \frac{c^2 (\rho - \rho_0)^2}{2\rho_0} d\mathbf{x}. \tag{32}$$

The kinetic energy E_{kin} can be further decomposed [34,44] as the sum of a *compressible* part $E^{\text{c}}_{\text{kin}}$ and an *incompressible* part $E^{\text{i}}_{\text{kin}}$:

$$E^{\text{c}}_{\text{kin}} = \int \frac{|(\sqrt{\rho}\mathbf{v})^{\text{c}}|^2}{2} d\mathbf{x}, \qquad E^{\text{i}}_{\text{kin}} = \int \frac{|(\sqrt{\rho}\mathbf{v})^{\text{i}}|^2}{2} d\mathbf{x}, \tag{33}$$

owing to the Helmholtz decomposition:

$$\begin{aligned} &(\sqrt{\rho}\mathbf{v}) = (\sqrt{\rho}\mathbf{v})^{\text{c}} + (\sqrt{\rho}\mathbf{v})^{\text{i}}, \quad \text{with } \nabla \times (\sqrt{\rho}\mathbf{v})^{\text{c}} = 0, \quad \text{and} \\ &\nabla \cdot (\sqrt{\rho}\mathbf{v})^{\text{i}} = 0. \end{aligned} \tag{34}$$

4.2. Spectra and structure functions

Spectra of the different components of the energy and structure functions of velocity will be used to analyse the QT field, as in CT. The energy spectra are computed using the following expressions resulting after applying Parseval's theorem for the Fourier transform:

$$\begin{aligned} E^{i}_{\text{kin}}(k) &= \frac{1}{2(2\pi)^3} \int_{|\mathbf{k}|=k} |\mathcal{F}_{\mathbf{k}}(\sqrt{\rho}\mathbf{v})^{i}|^2 \, d\Omega_{\mathbf{k}}, \\ E^{c}_{\text{kin}}(k) &= \frac{1}{2(2\pi)^3} \int_{|\mathbf{k}|=k} |\mathcal{F}_{\mathbf{k}}(\sqrt{\rho}\mathbf{v})^{c}|^2 \, d\Omega_{\mathbf{k}}, \\ E_{\text{int}}(k) &= \frac{c^2}{2\rho_0(2\pi)^3} \int_{|\mathbf{k}|=k} |\mathcal{F}_{\mathbf{k}}(\rho - \rho_0)|^2 \, d\Omega_{\mathbf{k}}, \\ E_{\text{q}}(k) &= \frac{c^2 \xi^2}{(2\pi)^3} \int_{|\mathbf{k}|=k} |\mathcal{F}_{\mathbf{k}}(\nabla \sqrt{\rho})|^2 \, d\Omega_{\mathbf{k}}, \end{aligned} \tag{35}$$

where $\mathcal{F}_{\mathbf{k}}$ is the Fourier transform

$$\mathcal{F}_{\mathbf{k}}(f(\mathbf{x})) = \int f(\mathbf{x}) e^{-i\mathbf{k}\cdot\mathbf{x}}\, d\mathbf{x}, \quad \mathcal{F}_{\mathbf{x}}^{-1}(g(\mathbf{k})) = \frac{1}{(2\pi)^3} \int g(\mathbf{k}) e^{i\mathbf{k}\cdot\mathbf{x}}\, d\mathbf{k}, \tag{36}$$

and $\Omega_{\mathbf{k}}$ is the solid angle in the spectral space.

The structure function for the velocity following the x-direction (with unitary vector $\mathbf{e}_x$) is defined as:

$$S_{/\!/}^p(r) = \int ((\mathbf{v}(\mathbf{x} + r\mathbf{e}_x) - \mathbf{v}(\mathbf{x})) \cdot \mathbf{e}_x)^p \, d\mathbf{x}, \tag{37}$$

where p is the order of the structure function and r the length scale. Similar expressions are used for the structure functions following the y and z directions. Assuming a homogeneous and isotropic distribution of the QT velocity field statistics, averaging over different directions should give the same results. As a verification, for $p = 2$ and large length scale r, the structure function could be reasonably approximated by:

$$\lim_{r\to\infty} S_{/\!/}^2(r) \simeq 2 \int |\mathbf{v}(\mathbf{x}) \cdot \mathbf{e}_x|^2 \, d\mathbf{x} = 2 \int v_x^2 \, d\mathbf{x}. \tag{38}$$

4.3. Helicity

The helicity is another important integral quantity characterizing the QT flow field. The definition of helicity in a classical flow is:

$$H = \int \mathbf{v} \cdot \boldsymbol{\omega} \, d\mathbf{x}, \tag{39}$$

where $\boldsymbol{\omega} = \nabla \times \mathbf{v}$ is the vorticity. In a quantum fluid, the vorticity concentrates in vortex cores as Dirac delta functions. Therefore, only quantized vortices bring a non-zero contribution to the helicity.

We use in this paper the method suggested by Clark di Leoni et al. [36] to compute the helicity. Because the superfluid velocity $\mathbf{v}$ diverges at the vortex cores as shown in Eq. (21), the direct calculation of the helicity looks ill-defined. However, only the superfluid velocity perpendicular to the quantized vortex has a singularity, while the component parallel to the quantized vortex remains regular. Using this observation, a regularized velocity is defined as:

$$\mathbf{v}_{\text{reg}} = v_{\parallel} \mathbf{w} / \sqrt{w_j w_j}, \tag{40}$$

where

$$\mathbf{w} = \frac{\hbar}{im} \nabla\psi^* \times \nabla\psi, \tag{41}$$

and

$$v_{\parallel} = \frac{\hbar\, w_i \left[(\partial_i\partial_j\psi)\partial_j\psi^* - (\partial_i\partial_j\psi^*)\partial_j\psi \right]}{2im\sqrt{w_k w_k}(\partial_l\psi)(\partial_l\psi^*)}. \tag{42}$$

The resultant regularized helicity

$$H_{\text{reg}} = \int \mathbf{v}_{\text{reg}} \cdot \boldsymbol{\omega} \, d\mathbf{x}, \tag{43}$$

proved useful and efficient in computing the helicity of quantum flows with hundreds of thousands of knots [36].

5. Numerical method and computational code

Numerical simulations were performed using the parallel code called GPS (Gross–Pitaevskii Simulator) [15]. The code is based on a Fourier-spectral space discretization and recent up-to-date numerical methods: a semi-implicit backward-Euler scheme with Krylov preconditioning for the stationary GP equation [16] and various schemes (Strang splitting, relaxation, Crank–Nicolson) for the real-time GP equation [17]. GPS is written in Fortran 90 and uses a two-level communication scheme based on MPI across nodes and OpenMP within nodes. Only one external library, FFTW [45], is required for the computation. Initially designed to simulate BEC configurations (with or without rotation), the GPS code was adapted in this study for the simulation of QT flows. We present in this section the main features of the numerical system: the particular scaling used to obtain the GP dimensionless equations, and the particular numerical methods used to prepare the initial state and then to advance in real-time the GP wave function.

5.1. Scaling and dimensionless equations

For the numerical resolution of the GP equation (1), it is convenient to use a dimensionless form obtained after scaling all physical quantities with the characteristic scales of the QT field introduced in Section 4. We start by considering general reference scales (L_{ref}, v_{ref}) for length and velocity, respectively. A natural scale for the wave function ψ is $\psi_{\text{ref}} = \sqrt{n_0}$. With the scaling:

$$\tilde{\mathbf{x}} = \frac{\mathbf{x}}{L_{\text{ref}}}, \quad \tilde{t} = \frac{v_{\text{ref}}}{L_{\text{ref}}} t, \quad \tilde{\psi} = \frac{\psi}{\sqrt{n_0}}, \tag{44}$$

the dimensionless GP equation (28) (with $V_{\text{trap}} = 0$) becomes:

$$i\frac{\partial}{\partial\tilde{t}}\tilde{\psi}(\mathbf{x}, t) = \left(-\alpha\tilde{\nabla}^2 + \beta\left(|\tilde{\psi}(\tilde{\mathbf{x}}, t)|^2 - 1 \right) \right) \tilde{\psi}(\mathbf{x}, t), \tag{45}$$

with non-dimensional coefficients:

$$\alpha = \frac{\hbar}{2m}\frac{1}{L_{\text{ref}}v_{\text{ref}}} = \frac{\sqrt{2}\xi c}{2}\frac{1}{L_{\text{ref}}v_{\text{ref}}} = \frac{1}{\sqrt{2}}\left(\frac{\xi}{L_{\text{ref}}}\right)\left(\frac{c}{v_{\text{ref}}}\right), \tag{46}$$

$$\beta = \frac{gn_0}{\hbar}\frac{L_{\text{ref}}}{v_{\text{ref}}} = \frac{mc^2}{\hbar}\frac{L_{\text{ref}}}{v_{\text{ref}}} = \frac{c^2}{\sqrt{2}\xi c}\frac{L_{\text{ref}}}{v_{\text{ref}}} = \frac{1}{\sqrt{2}}\left(\frac{L_{\text{ref}}}{\xi}\right)\left(\frac{c}{v_{\text{ref}}}\right). \tag{47}$$

From (46)–(47) we infer that non-dimensional coefficients α and β are related to physically relevant scales through:

$$\tilde{\xi} = \frac{\xi}{L_{\text{ref}}} = \sqrt{\frac{\alpha}{\beta}}, \quad \tilde{c} = \frac{c}{v_{\text{ref}}} = \sqrt{2\alpha\beta} = \frac{1}{M_{\text{ref}}}, \tag{48}$$

where (ξ/L_{ref}) represents the non-dimensional healing length and (c/v_{ref}) the non-dimensional sound velocity. M_{ref} is the reference Mach number, defined as the ratio between the reference velocity and the sound velocity.

The last important parameters to define when working with non-dimensional equations are the size of the computational box and the grid resolution. If the physical GP equation (1) is defined in a cubic computational domain of physical size L, the non-dimensional size $\mathcal{L}$ of the computational box used to discretize the non-dimensional equation (45) is then:

$$\mathcal{L} = \frac{L}{L_{\text{ref}}} = \left(\frac{L}{\xi}\right)\left(\frac{\xi}{L_{\text{ref}}}\right) = \left(\frac{L}{\xi}\right)\sqrt{\frac{\alpha}{\beta}}. \tag{49}$$

We recall that ξ is a good approximation of the radius of a quantum vortex (see Section 3.2). It follows that the ratio (L/ξ) in (49) is physically important since it indicates how many vortices the computational domain can accommodate in one direction:

$$N_v^{1d} = \frac{L}{2\xi} = \frac{\mathcal{L}}{2}\sqrt{\frac{\beta}{\alpha}}. \tag{50}$$

Thus, increasing the value of $\mathcal{L}$ (for fixed α and β) will result in a higher number of vortices present in the computational box.

When defining the grid resolution, it is important to control the number of grid points inside the vortex core. If the numerical simulation uses N_x grid points in each direction, the physical grid spacing is $\delta x = L/N_x$, or in non-dimensional units $\delta\tilde{x} = (\delta x/L_{\text{ref}}) = \mathcal{L}/N_x$. It is important to quantify the grid spacing with respect to the healing length by defining:

$$\chi = \frac{\delta x}{\xi} = \left(\frac{\mathcal{L}}{N_x}\right)\left(\frac{L_{\text{ref}}}{\xi}\right) = \left(\frac{\mathcal{L}}{N_x}\right)\sqrt{\frac{\beta}{\alpha}}. \tag{51}$$

The parameter χ defined in (51) is also important when analysing the dispersion relation (26) presented in Section 3.3 to assess on the validity of the GP model. Indeed, the maximum wave-number represented on a grid of size δx is $k_{max} = (2\pi)/(2\delta x)$ and, consequently, the non-dimensional quantity $(k_{max}\xi)$ is expressed as:

$$k_{max}\xi = \pi\frac{\xi}{\delta x} = \frac{\pi}{\chi}. \tag{52}$$

The numerical resolution will be then fixed in order to keep $(k_{max}\xi) \approx 1$, ensuring that the simulation captures the regime of phonons excitations.

We use in this paper the strategy suggested in [34,44] to fix the values of parameters defining a QT simulation. The size of the non-dimensional computational box is first set to $\mathcal{L} = 2\pi$, which is convenient for spectral methods. Moreover, instead of setting independently the constants α and β, only the value of the reference Mach number M_{ref} is fixed to a relatively low value. This is equivalent to impose the value of the product $\alpha\beta$. From previous relations we infer that:

$$\mathcal{L} = 2\pi, \quad \alpha\beta = \frac{1}{2M_{\text{ref}}^2} \Longrightarrow \begin{cases} \dfrac{\xi}{L_{\text{ref}}} &= \sqrt{2}\alpha M_{\text{ref}}, \\ v_{\text{ref}} &= M_{\text{ref}}c, \\ \dfrac{L}{\xi} &= \dfrac{2\pi}{\sqrt{2}\alpha M_{\text{ref}}}, \\ k_{max}\xi &= \left(\dfrac{N_x}{2}\right)\sqrt{2}\alpha M_{\text{ref}}. \end{cases} \tag{53}$$

We note from (53) that the parameter α can be used to control the non-dimensional size of the vortex, while the grid resolution N_x can be set to control the parameter $(k_{max}\xi)$. We generally set for QT simulations $M_{\text{ref}} = 0.5$, equivalent to $\alpha\beta = 2$.

Particular care has to be devoted when computing non-dimensional values of different quantities appearing in integral invariants or in the hydrodynamic analogy. If the non-dimensional wave function is computed from (45) as $\tilde{\psi}(\tilde{\mathbf{x}}, \tilde{t}) = |\tilde{\psi}|\exp(i\theta(\tilde{\mathbf{x}}, \tilde{t}))$, the scaled number of atoms results from (4) as:

$$\tilde{N} = \frac{N}{N_0} = \frac{1}{\mathcal{L}^3}\int_{\mathcal{D}} |\tilde{\psi}|^2 d\tilde{\mathbf{x}}, \tag{54}$$

where $\mathcal{D}$ is the non-dimensional computation domain. The scaled total energy (per volume unit) results from (27):

$$\tilde{E}(\tilde{\psi}) = \frac{E_T(\psi)}{E_{\text{ref}}} = \frac{2\alpha}{\mathcal{L}^3}\int_{\mathcal{D}}\left(\alpha|\tilde{\nabla}\tilde{\psi}|^2 + \frac{\beta}{2}\left(|\tilde{\psi}|^2 - 1\right)^2\right) d\tilde{\mathbf{x}}, \tag{55}$$

with energy units $E_{\text{ref}} = \rho_0 v_{\text{ref}}^2 L^3 = \hbar^2 n_0 L\mathcal{L}^2/(4m\alpha^2)$.

From the hydrodynamic analogy developed in Section 2, taking as reference the density of the background uniform flow, *i.e.* $\rho_{\text{ref}} = \rho_0 = mn_0$, results in:

$$\tilde{\rho} = \frac{\rho}{\rho_{\text{ref}}} = \frac{mn_0|\tilde{\psi}|^2}{\rho_{\text{ref}}} = |\tilde{\psi}|^2. \tag{56}$$

The momentum is derived from (10) and thus computed in the non-dimensional code as:

$$\tilde{\rho}\tilde{\mathbf{v}}(\tilde{\mathbf{x}}, \tilde{t}) = 2\alpha \frac{\tilde{\psi}^*\tilde{\nabla}\tilde{\psi} - \tilde{\psi}\tilde{\nabla}\tilde{\psi}^*}{2i} = (2\alpha)\mathcal{I}mag(\tilde{\psi}^*\tilde{\nabla}\tilde{\psi}). \tag{57}$$

The non-dimensional superflow velocity also results from (10):

$$\tilde{\mathbf{v}}(\tilde{\mathbf{x}}, \tilde{t}) = \frac{\mathbf{v}(\mathbf{x}, t)}{v_{\text{ref}}} = \frac{\hbar}{mv_{\text{ref}}L_{\text{ref}}}\tilde{\nabla}\theta(\tilde{\mathbf{x}}, \tilde{t}) = 2\alpha\,\tilde{\nabla}\theta(\tilde{\mathbf{x}}, \tilde{t}), \tag{58}$$

and the non-dimensional circulation of a vortex of winding number ($\kappa = 1$) from (22):

$$\tilde{\Gamma} = \frac{\Gamma_v}{v_{\text{ref}}L_{\text{ref}}} = 2\pi\frac{\hbar}{mv_{\text{ref}}L_{\text{ref}}} = 4\pi\alpha. \tag{59}$$

Finally, the hydrodynamic expression (29) of the total energy becomes

$$\begin{aligned}\tilde{E}(\tilde{\psi}) &= \frac{E_T(\psi)}{E_{\text{ref}}} \\ &= \frac{1}{\mathcal{L}^3}\int_{\mathcal{D}}\left(\frac{1}{2}\tilde{\rho}\tilde{\mathbf{v}}^2 + (2\alpha^2)|\nabla(\sqrt{\tilde{\rho}})|^2 + (\alpha\beta)(\tilde{\rho}-1)^2\right)d\tilde{\mathbf{x}},\end{aligned} \tag{60}$$

with the same reference energy as in (55) $E_{\text{ref}} = \rho_0 v_{\text{ref}}^2 L^3$. In (60) the first term represents the kinetic energy $\tilde{E}_{kin}(\tilde{\psi})$, the second the quantum energy $\tilde{E}_q(\tilde{\psi})$ and the third the interaction energy $\tilde{E}_{int}(\tilde{\psi})$. Note that $2\alpha^2 = \tilde{\xi}^2\tilde{c}^2$ and $\alpha\beta = 1/(2M_{\text{ref}}^2)$.

To simplify the presentation, we drop in the following the tilde notation. All the developments and results in the remaining of the paper concern non-dimensional quantities.

5.2. Numerical method to compute stationary solutions

To find stationary solutions to (45), a very popular numerical method is the *normalized gradient flow* [46]. The wave function is propagated (in *imaginary time*) following the gradient flow corresponding to the minimization of the energy (55), until a local or global minimum of the energy is reached, corresponding to metastable or ground states, respectively. In the original method, the solution is subsequently normalized to satisfy the constraint of the conservation of the number of atoms (equivalent to imposing the L^2-norm of the solution). In our case, we want to find a stationary state that mimics a classical flow with prescribed velocity $\mathbf{v}_{\text{ext}}$. Assuming that $\nabla\cdot\mathbf{v}_{\text{ext}} = 0$, after applying a local Galilean transformation, the non-dimensional energy of the driven field becomes [see34, for details]:

$$E_{\mathbf{v}} = \frac{2\alpha}{\mathcal{L}^3}\int_{\mathcal{D}}\left(\alpha\left|\nabla\psi - i\frac{\mathbf{v}_{\text{ext}}}{2\alpha}\psi\right|^2 + \frac{\beta}{2}(|\psi|^2-1)^2\right)d\mathbf{x}, \tag{61}$$

or, using the hydrodynamic analogy:

$$E_{\mathbf{v}}(\psi) = \frac{1}{\mathcal{L}^3}\int_{\mathcal{D}}\left(\frac{1}{2}\rho\,|\mathbf{v}-\mathbf{v}_{\text{ext}}|^2 + (2\alpha^2)\left|\nabla(\sqrt{\rho})\right|^2 + (\alpha\beta)(\rho-1)^2\right)d\mathbf{x}. \tag{62}$$

In this setting, we are searching an unconstrained minimizer of $E_{\mathbf{v}}$. Owing to the previous decomposition, there is a competition between the background uniform distribution $|\psi|^2 = 1$ and a phase accommodating to $\mathbf{v}_{\text{ext}}$. Numerically, we solve the gradient descent equation (or Advective Real Ginzburg–Landau Equation, ARGLE):

$$\frac{\partial}{\partial\tau}\phi(\mathbf{x}, t) = \left(\alpha\nabla^2 - i\mathbf{v}_{\text{ext}}\cdot\nabla - \frac{|\mathbf{v}_{\text{ext}}|^2}{4\alpha} + \beta - \beta|\phi(\mathbf{x}, t)|^2\right)\phi(\mathbf{x}, t), \quad \mathbf{x}\in\mathcal{D}, \tag{63}$$

with initial condition $\phi(\mathbf{x}, 0^+) = \phi_0(\mathbf{x})$. Note that τ is here a pseudo-time used to propagate the solution until a stationary state is reached. Hence, this method belongs to the class of so-called *imaginary time propagation* methods. We use a semi-implicit Backward Euler scheme to advance the solution in the pseudo-time interval (τ_n, τ_{n+1}):

$$\frac{\tilde{\phi}^{n+1}(\mathbf{x}) - \phi^n(\mathbf{x})}{\delta\tau} = \frac{\alpha}{2}\nabla^2\tilde{\phi}^{n+1} + \left(\frac{\alpha}{2}\nabla^2 - i\mathbf{v}_{\text{ext}}\cdot\nabla - \frac{|\mathbf{v}_{\text{ext}}|^2}{4\alpha} + \beta - \beta|\phi^n(\mathbf{x})|^2\right)\tilde{\phi}^n(\mathbf{x}). \tag{64}$$

where $\delta\tau := \tau_{n+1} - \tau_n$. The resulting system is solved with spectral accuracy using FFTs. The Backward Euler scheme was proved to be very effective is solving stationary GP equations with spectral discretization (the terms in Eq. (64) are easily computed with FFTs). The details of the spectral implementation and some proofs for the energy diminishing properties of the scheme are provided in [46].

The ARGLE procedure stops either after a pre-definite number of pseudo-time steps or when the convergence criterion is reached:

$$\frac{\|\phi^{n+1} - \phi^n\|_\infty}{\delta\tau} \le \epsilon, \tag{65}$$

where ϵ is a user defined parameter. If this criterion is not satisfied at the end of the computation, it is still possible to check the energy convergence condition:

$$\frac{|E_{\mathbf{v}}(\phi^{n+1}) - E_{\mathbf{v}}(\phi^n)|}{\delta\tau E_{\mathbf{v}}(\phi^n)} \leq \epsilon, \tag{66}$$

which is generally less constraining than (65). Note that, even when the convergence is achieved, we can only guarantee that the *Backward Euler method* provides a local minimum of $E_{\mathbf{v}}$.

5.3. Numerical method for the time evolution

The simulation of QT consists of solving the GP equation (45) using a pseudo-spectral scheme in space and a second order splitting for the time discretization (ADI, Alternating Direction Implicit or Strang splitting). Let us rewrite (45) as:

$$\begin{aligned}\frac{\partial}{\partial t}\psi &= i\alpha\Delta\psi - i\beta|\psi|^2\psi \\ &= \mathcal{L}_x\psi + \mathcal{L}_y\psi + \mathcal{L}_z\psi + N(\psi),\end{aligned} \tag{67}$$

with the following definitions:

$$\begin{aligned}\mathcal{L}_x\psi &= i\alpha\partial^2_{xx}\psi, & \mathcal{L}_y\psi &= i\alpha\partial^2_{yy}\psi, \\ \mathcal{L}_z\psi &= i\alpha\partial^2_{zz}\psi, & N(\psi) &= -i\beta|\psi|^2\psi.\end{aligned} \tag{68}$$

If H denotes one of the previous operators ($\mathcal{L}_x$, $\mathcal{L}_y$, $\mathcal{L}_z$ or N), and ϕ is a given field, we denote by $S(s,H)\phi := \psi(s)$ the solution at time $t = s$ of the following Cauchy problem:

$$\begin{cases}\dfrac{\partial}{\partial t}\psi & = H(\psi), \\ \psi(t=0) & = \phi.\end{cases} \tag{69}$$

Then the second order Strang splitting scheme is:

$$\psi_{n+1} = S\left(\frac{\delta t}{2}, \mathcal{L}_x\right) S\left(\frac{\delta t}{2}, \mathcal{L}_y\right) S\left(\frac{\delta t}{2}, \mathcal{L}_z\right) S(\delta t, N) S\left(\frac{\delta t}{2}, \mathcal{L}_z\right) S\left(\frac{\delta t}{2}, \mathcal{L}_y\right) S\left(\frac{\delta t}{2}, \mathcal{L}_x\right) \psi_n. \tag{70}$$

This scheme is indeed second order accurate, provided that we solve the partial problems exactly, *i.e.* each term $S(s,H)$ is computed exactly. This is achieved using the spectral representation. For $j \in \{x,y,z\}$, using $\mathcal{F}_j$ the Fourier transform in the j direction, we obtain

$$S\left(s, \mathcal{L}_j\right)\phi = \mathcal{F}_j^{-1}\left(e^{-i\alpha k_j^2 s}\mathcal{F}_j\phi\right). \tag{71}$$

For the non linear operator $S(\delta t, N)$, we notice that, if ψ^N is such that $\partial_t\psi^N = -i\beta|\psi^N|^2\psi^N$, then $\partial(|\psi^N|^2)/\partial t = 0$. Consequently, this step can be solved analytically and:

$$S\left(s, N\right)\phi = e^{-i\beta|\phi|^2 s}\phi. \tag{72}$$

In conclusion, using the spectral discretization we obtain a second order accurate scheme for the time integration.

6. Initial data preparation and benchmarks

As in numerical studies of classical turbulence, the preparation of the initial state is crucial in investigating statistical properties of QT. We describe in this section four different approaches to generate the initial field for the simulation of decaying GP-QT. Each method is associated to a benchmark for the GP-QT simulation. The first two methods are classical [34,44] and inspired from CT. They start from defining a velocity field containing vortices. The Taylor–Green or the Arnold–Beltrami–Childress (ABC) model flows are used for this step. A wave function field is then constructed such that its nodal lines correspond to vortex lines of the velocity field. This initial wave function is then used in the ARGLE procedure described in Section 5.2 to generate an initial field for the real-time GP simulations. The role of the ARGLE step is to reduce the acoustic emission of the initial field. The last two methods are new and based on the direct manipulation of the wave function. We prescribe either a random phase field or we manufacture an initial field containing many quantum vortex rings. The four methods are described in detail below.

6.1. Taylor–Green (TG) flow

The velocity $\mathbf{v}_{\mathrm{TG}}$ of the Taylor–Green (TG) three-dimensional vortex flow is defined as:

$$\begin{aligned}v_{\mathrm{TG},x}(x,y,z) &= \sin(x)\cos(y)\cos(z), \\ v_{\mathrm{TG},y}(x,y,z) &= -\cos(x)\sin(y)\cos(z), \\ v_{\mathrm{TG},z}(x,y,z) &= 0.\end{aligned} \tag{73}$$

To create a wave function field ψ_{TG} with zeros along vortex lines of $\mathbf{v}_{\mathrm{TG}}$, we make use of the Clebsch representation of the velocity field [34,44]:

$$\nabla\times\mathbf{v}_{\mathrm{TG}} = \nabla\lambda\times\nabla\mu, \tag{74}$$

with Clebsch potentials

$$\begin{aligned}\lambda(x,y,z) &= \cos(x)\sqrt{2\,|\cos(z)|},\\ \mu(x,y,z) &= \cos(y)\sqrt{2\,|\cos(z)|}\,\mathrm{sgn}(\cos(z)),\end{aligned} \tag{75}$$

where sgn is the sign function. Note that a zero in the (λ,μ) plane corresponds to a vortex line of $\mathbf{v}_{\mathrm{TG}}$ (see [34,44] for details).

In practice, we start by defining in the (λ,μ) plane a complex field ψ_e with a simple zero at the origin:

$$\psi_e(\lambda,\mu) = (\lambda+i\mu)\frac{\tanh(\sqrt{\lambda^2+\mu^2}/\sqrt{2}\xi)}{\sqrt{\lambda^2+\mu^2}}. \tag{76}$$

When replacing (75) into (76), a three-dimensional complex field is obtained, with one nodal line. We can further define on $[0,\pi]^3$:

$$\begin{aligned}\psi_4(x,y,z) &= \psi_4(\lambda(x,y,z),\mu(x,y,z))\\ &= \psi_e(\lambda-\frac{1}{\sqrt{2}},\mu)\psi_e(\lambda,\mu-\frac{1}{\sqrt{2}})\psi_e(\lambda+\frac{1}{\sqrt{2}},\mu)\psi_e(\lambda,\mu+\frac{1}{\sqrt{2}}),\end{aligned} \tag{77}$$

which now contains four nodal lines (see Fig. 1a, left). When ψ_e is extended by mirror reflection to the entire domain $[0,2\pi]^3$, the obtained wave function field contains closed rings inside the domain (see Fig. 1a, right).

The last manipulation of the wave function is intended to match the circulation of the velocity field $\mathbf{v}_{\mathrm{TG}}$. From (74) and (75) we compute the circulation on the face $z=0$, $(x,y)\in[0,\pi]\times[0,\pi]$ using the Stokes' theorem:

$$\begin{aligned}\Gamma_{z=0} &= \int_0^\pi\int_0^\pi (\nabla\times\mathbf{v}_{\mathrm{TG}})\cdot\mathbf{e}_z\,dx\,dy\\ &= \int_0^\pi\int_0^\pi 2\sin(x)\sin(y)dx\,dy = 8.\end{aligned} \tag{78}$$

Defining the ratio of the total circulation to the circulation (59) of a single vortex as $\gamma_d = \Gamma/\Gamma_v = 2/(\pi\alpha)$, the wave-function field matching the circulation of the TG velocity field is [34] is

$$\psi_{\mathrm{ARGLE}}(x,y,z) = \psi_4(\lambda(x,y,z),\mu(x,y,z))^{[\gamma_d/4]}, \tag{79}$$

where [.] denotes the integer part. In this setting, each vortex line corresponds to a multiple zero line (see Fig. 1a). The next step in the preparation of the initial field is to use the ARGLE imaginary time procedure (63) with $\mathbf{v}_{\mathrm{ext}} = \mathbf{v}_{\mathrm{TG}}$ and initial condition $\phi(t=0^+) = \psi_{\mathrm{ARGLE}}$. During the ARGLE dynamics the multiple zero lines in ψ_{ARGLE} will spontaneously split into $[\gamma_d/4] = [1/(2\pi\alpha)]$ single zero lines (see Fig. 1b). The system will finally converge to initial conditions for the GPE, compatible with the TG flow, and with minimal sound emission. We denote the resulting converged state as ϕ_{TG} (see Fig. 1c).

6.2. Arnold–Beltrami–Childress (ABC) flow

The TG vortex flow (73) has zero helicity. To obtain a helical flow at large scales, we use the method suggested by Clark di Leoni et al. [37] in their study of helical quantum turbulence at zero temperature. The external velocity field is defined as the superposition of two Arnold–Beltrami–Childress (ABC) flows:

$$\mathbf{v}_{\mathrm{ABC}} = \mathbf{v}^{(1)}_{\mathrm{ABC}} + \mathbf{v}^{(2)}_{\mathrm{ABC}}, \tag{80}$$

with

$$\begin{aligned}v^{(k)}_{\mathrm{ABC},x}(x,y,z) &= B\cos(ky) + C\sin(kz),\\ v^{(k)}_{\mathrm{ABC},y}(x,y,z) &= C\cos(kz) + A\sin(kx),\\ v^{(k)}_{\mathrm{ABC},z}(x,y,z) &= A\cos(kx) + B\sin(ky).\end{aligned} \tag{81}$$

Unless stated otherwise, we use $(A,B,C) = (0.9,1,1.1)/\sqrt{3}$. As for the Taylor–Green flow, we use the ARGLE procedure (63) with $\mathbf{v}_{\mathrm{ext}} = \mathbf{v}_{\mathrm{ABC}}$ and initial condition:

$$\phi(t=0^+) = \psi^{(1)}_{\mathrm{ABC}}\times\psi^{(2)}_{\mathrm{ABC}}. \tag{82}$$

The wave functions ψ_{ABC} are defined as:

$$\begin{aligned}\psi^{(k)}_{\mathrm{ABC}} &= \psi^{x,y,z}_{A,k}\times\psi^{y,z,x}_{B,k}\times\psi^{z,x,y}_{C,k}, \quad \psi^{x,y,z}_{A,k}\\ &= \exp\left(i\left[\frac{A\sin(kx)}{2\alpha}\right]y + i\left[\frac{A\cos(kx)}{2\alpha}\right]z\right),\end{aligned} \tag{83}$$

where $[a]$ stands for the nearest integer to a. The ARGLE procedure has the role to minimize the amount of energy of acoustic modes in the initial condition. Details of the quantum ABC flow are discussed by Clark di Leoni et al. [36,37]. We denote the resulting converged state as ϕ_{ABC}.

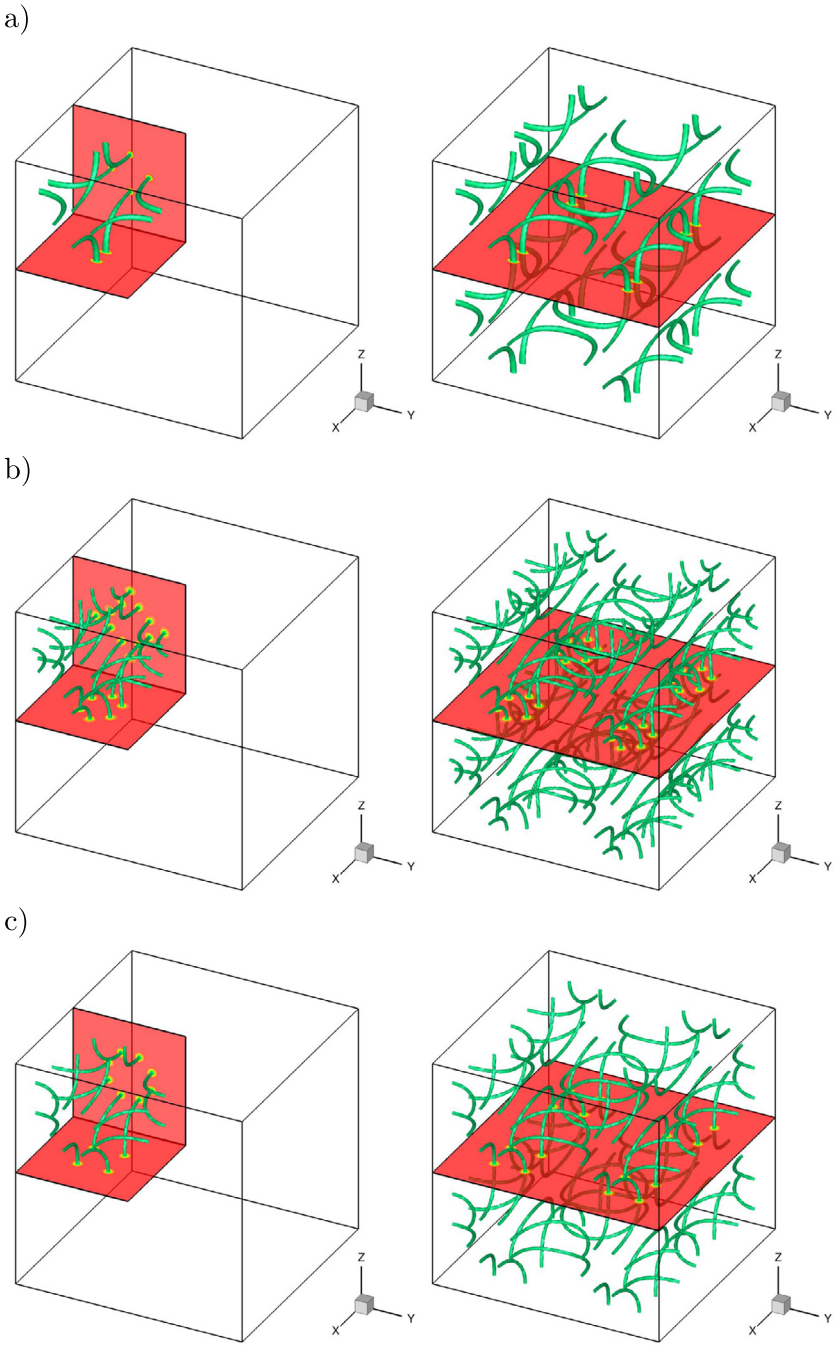

Fig. 1. Illustration of the initial field preparation using the Taylor–Green vortex flow. Imaginary time evolution of quantized vortices (iso-surfaces of low ϕ_{TG}) during the ARGLE calculation. Case $N_x = 128$ with $[\gamma_d/4] = 3$ (see Table 2). Two different views, on the subdomain $[0, \pi]^3$ (left) and the entire domain $[0, 2\pi]^3$ (right), illustrating the symmetry of the flow. Panels from top to bottom: (a) $\tau = 0$, the initial condition $\phi(t = 0^+) = \psi_{\mathrm{ARGLE}}$, Eq. (79) with multiply quantized (thick) vortices, (b) $\tau = 1$ when each initial vortex line splits in 3 singly quantized vortices and (c) $\tau = 60$ for the final converged ARGLE field, with closed loops inside the domain.

6.3. Smoothed random phase (SRP) initial wave function field

Previous initial fields for the simulation of the QT were built based on the analogy with classical flows (TG and ABC) with vortices. We present in this section the first method to set an initial field by direct manipulation of the wave function. A smoothed random phase (SRP) is assigned to the initial wave function ψ_{SRP}. Initially, there are no vortices present in the field. Vortices nucleate during the time evolution and their interaction generate a QT field. In practice, to obtain the nucleation of enough vortices for QT, we initialize the field as follows:

$$\psi_{\mathrm{SRP}} = e^{i\theta(\mathbf{x})}, \tag{84}$$

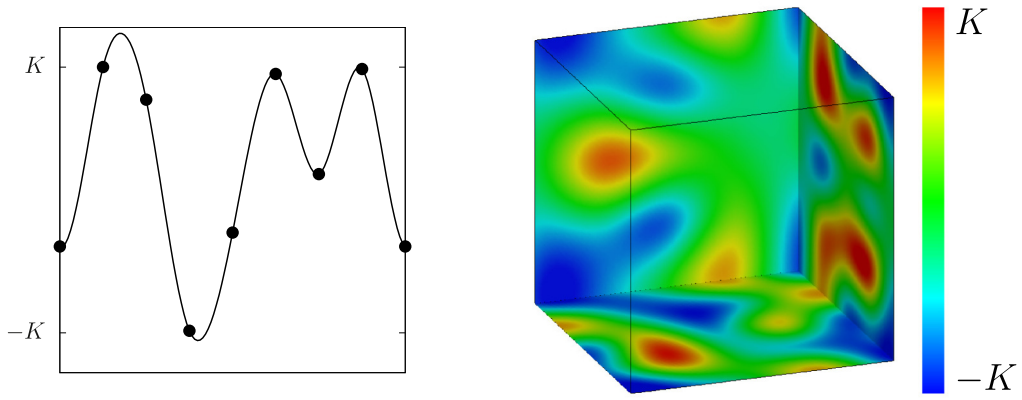

Fig. 2. Illustration of the initial field preparation using the SRP (smoothed random phase) method. Spline interpolation in one dimension using random values for the phase (left) and density contours (right) of the final 3D wave function ψ_{SRP}.

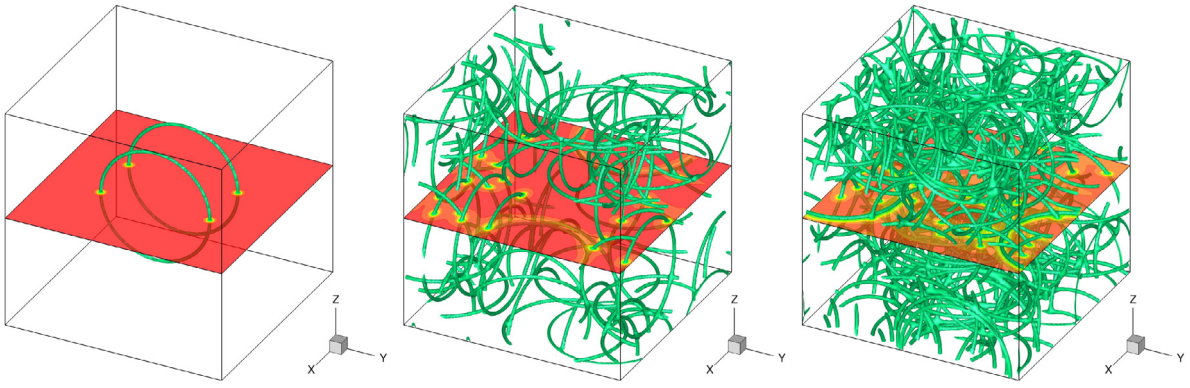

Fig. 3. Illustration of the initial field preparation using random vortex ring pairs. Vortex lines (iso-surfaces of low ρ) for the wave function ψ_{RVR} (Eq. (99)) with, from left to right, $N_{\text{V}} = 1$, 20 and 50 vortex ring pairs.

where θ is a smooth random periodic function in the computational box. To create this initial phase, we first generate the random phase $\theta_{i,j,k} \in [-K, K]$ at N_r^3 points $\mathbf{x}_{i,j,k} = N_s \times (i, j, k)$ where $N_s = N/N_r$ and $i, j, k \in \{0, 1, 2, \ldots, N_r - 1\}$. Then, θ is obtained by cubic spline interpolation (with periodicity) using the points $(\mathbf{x}_{i,j,k}, \theta_{i,j,k})$. The one-dimensional cubic (and uniform) spline interpolation is expressed as:

$$\begin{aligned}
&\theta_{N_s i_r + i_s, N_s j_r, N_s k_r} = A_{i_s}\theta_{N_s i_r, N_s j_r, N_s k_r} + B_{i_s}\theta_{N_s(i_r+1), N_s j_r, N_s k_r} + C_{i_s}\theta''_{N_s i_r, N_s j_r, N_s k_r} + D_{i_s}\theta''_{N_s(i_r+1), N_s j_r, N_s k_r},\\
&A_{i_s} = \frac{N_s - i_s}{N_s}, \quad B_{i_s} = \frac{i_s}{N_s}, \quad C_{i_s} = \frac{(A_{i_s}^3 - A_{i_s})N_s^2}{6},\\
&D_{i_s} = \frac{(B_{i_s}^3 - B_{i_s})N_s^2}{6},
\end{aligned} \tag{85}$$

for $i_r, j_r, k_r \in \{0, 1, \ldots, N_r - 1\}$ and $i_s \in \{1, 2, \ldots, N_s - 1\}$. The second derivative θ'' is obtained by solving the following linear system with tridiagonal matrix:

$$N_s^2(\theta''_{N_s i_r - 1, N_s j_r, N_s k_r} + 4\theta''_{N_s i_r, N_s j_r, N_s k_r} + \theta''_{N_s i_r + 1, N_s j_r, N_s k_r}) = 6\left(\theta_{N_s i_r - 1, N_s j_r, N_s k_r} - 2\theta_{N_s i_r, N_s j_r, N_s k_r} + \theta_{N_s i_r + 1, N_s j_r, N_s k_r}\right). \tag{86}$$

After the interpolation along the i-direction, we compute the spline interpolation along the j-direction

$$\theta_{i, N_s j_r + j_s, N_s k_r} = A_{j_s}\theta_{i, N_s j_r, N_s k_r} + B_{j_s}\theta_{i, N_s(j_r+1), N_s k_r} + C_{j_s}\theta''_{i, N_s j_r, N_s k_r} + D_{j_s}\theta''_{i, N_s(j_r+1), N_s k_r}, \tag{87}$$

for $i \in \{0, 1, \ldots, N - 1\}$, $j_r, k_r \in \{0, 1, \ldots, N_r - 1\}$, and $j_s \in \{1, 2, \ldots, N_s - 1\}$, and, finally, that along the k-direction

$$\theta_{i,j,N_s k_r + k_s} = A_{k_s}\theta_{i,j,N_s k_r} + B_{k_s}\theta_{i,j,N_s(k_r+1)} + C_{k_s}\theta''_{i,j,N_s k_r} + D_{k_s}\theta''_{i,j,N_s(k_r+1)}, \tag{88}$$

for $i, j \in \{0, 1, \ldots, N - 1\}$, $k_r \in \{0, 1, \ldots, N_r - 1\}$, and $k_s \in \{1, 2, \ldots, N_s - 1\}$.

With this method, the characteristic variation of the phase θ is KN_r/π. The characteristic velocity results from (58): $v = 2\alpha(KN_r/\pi)$. The Mach number of the system is computed using (48) as $M = v/c = \sqrt{2\alpha}KN_r/\pi\sqrt{\beta}$.

We denote the resulting converged state as ψ_{SRP}. An example of the resulting flow is shown in Fig. 2.

6.4. Random vortex rings (RVR) initial wave function field

The main idea for this last initial condition is to prepare an initial state containing enough vortices to lead to QT. We derive in the following a method to fill the computational bow with vortex rings. The challenge is to obtain a physically acceptable ansatz. We start from the single vortex ring solution to the GP equation [38]. A vortex ring of radius R and constant translational speed can be approximated as:

$$\psi_{\mathrm{VR}}(x,y,z,R) = f\left(\sqrt{(r-R)^2+\tilde{z}^2}\right) e^{\pm i \tan^{-1}\left(\frac{\tilde{z}}{r-R}\right)}, \tag{89}$$

$$f(r) = \sqrt{\frac{a_1(r/\xi)^2 + a_2(r/\xi)^4}{1+b_1(r/\xi)^2+a_2(r/\xi)^4}}, \tag{90}$$

$$a_1 = \frac{73+3\sqrt{201}}{352}, \quad a_2 = \frac{6+\sqrt{201}}{528},$$

$$b_1 = \frac{21+\sqrt{201}}{96}, \tag{91}$$

$$\tilde{\mathbf{x}} = \mathbf{x} - \pi, \tag{92}$$

$$r = \sqrt{\tilde{x}^2+\tilde{y}^2}, \tag{93}$$

$$\xi = \sqrt{\alpha/\beta} \tag{94}$$

where $f(r)$ is the solution to the GP equation (45) written in cylindrical coordinates for $\psi = f(r)e^{i\kappa \tan^{-1}(y/x)}$ with $\kappa = 1$:

$$-\frac{\alpha}{r}\frac{d}{dr}\left(r\frac{df}{dr}\right) + \frac{\alpha\kappa^2 f}{r^2} + \beta(f^2-1)f = 0. \tag{95}$$

The form in (90) is obtained as the Padé approximation of this solution. Coefficients a_1, a_2, and b_1 in (91) are fixed by satisfying (95) to the order of $(r/\xi)^3$ for both $r/\xi \ll 1$ and $r/\xi \gg 1$. This expression stands for a vortex ring centred in the origin. Note that this definition is consistent with a vortex core size of the order of ξ.

The vortex ring ansatz ψ_{R} has the finite net momentum $\rho\mathbf{v}$. To eliminate this momentum, we add an opposite-symmetrical ring by setting the wave function for a vortex-ring pair (VRP) as:

$$\psi_{\mathrm{VRP}}(x,y,z,R,d) = \psi_{\mathrm{VR}}(x,y,z-d/2,R)\psi^*_{\mathrm{VR}}(x,y,z+d/2,R), \tag{96}$$

where d is the inter-vortex distance. Because the ansatz ψ_{VRP} for a vortex-ring pair does not satisfy the periodic boundary condition, we rewrite it as

$$\begin{aligned}\psi_{\mathrm{VRP}}(x,y,z,R,d) \rightarrow\ & \psi_{\mathrm{VRP}}(x,y,z,R,d)\\ & \times \psi^*_{\mathrm{VRP}}(2\mathcal{L}-x,y,z,R,d)\,\psi^*_{\mathrm{VRP}}(-x,y,z,R,d)\\ & \times \psi^*_{\mathrm{VRP}}(x,2\mathcal{L}-y,z,R,d)\,\psi^*_{\mathrm{VRP}}(x,-y,z,R,d)\\ & \times \psi^*_{\mathrm{VRP}}(x,y,2\mathcal{L}-z,R,d)\,\psi^*_{\mathrm{VRP}}(x,y,-z,R,d).\end{aligned} \tag{97}$$

The last step to prepare the initial state ψ_{RVR} (random vortex rings) is obtained by randomly putting vortex-ring pairs in the domain. First, we randomly translate the ansatz ψ_{VRP} (97) as

$$\psi_{\mathrm{RVR}}(x,y,z,R,d) \equiv \mathcal{F}^{-1}_{\mathbf{x}}\left(e^{i\mathbf{k}\cdot\mathbf{X}}\mathcal{F}_{\mathbf{k}}(\psi_{\mathrm{VRP}}(x,y,z,R,d))\right), \tag{98}$$

where $\mathbf{X} = (X,Y,Z) \in [0,2\pi]^3$ are uniform random numbers. After that, we randomly rotate the ansatz by:

$$\psi_{\mathrm{RVR}}(x,y,z,R,d) \rightarrow \left\{\begin{array}{c}\psi_{\mathrm{RVR}}(x,y,z,R,d)\\ \psi_{\mathrm{RVR}}(x,z,y,R,d)\\ \psi_{\mathrm{RVR}}(y,x,z,R,d)\\ \psi_{\mathrm{RVR}}(y,z,x,R,d)\\ \psi_{\mathrm{RVR}}(z,x,y,R,d)\\ \psi_{\mathrm{RVR}}(z,y,x,R,d)\end{array}\right\}. \tag{99}$$

Finally, the initial state ψ_{RPR} is obtained by preparing N_{V} different ansatze ψ_{RVR} and multiplying them. Changing the radius of the ring R, the inter-vortex distance d or the number of vortex rings pairs N_{V} will impact the behaviour of QT. An example of the resulting flow is shown in Fig. 3.

7. Numerical results

We describe in this section quantum turbulence flows simulated using the four initial conditions described in the previous section: Taylor–Green (TG), Arnold–Beltrami–Childress (ABC), smoothed random phase (SRP) and random vortex rings (RVR). We present values, spectra and structure functions of main quantities of interest (energy, helicity, etc.) that could be useful to benchmark numerical codes simulating QT.

The main physical and numerical parameters of the runs were fixed following the scaling analysis provided in Section 5.1 and are summarized in Table 1. Runs are identified using the abbreviation of the initial condition, followed by the identifier of the space resolution, *e.g.* TG_a is the run using the Taylor–Green initial condition and a 128^3 grid. Resolutions up to 1024^3 grid points (runs "_d")

Table 1
Numerical and physical parameters used in the QT simulations.

Run	$\mathcal{L}$	N_x	M_{ref}	c	α	β	$k_{max}\xi$	$\delta x/\xi$	ξ	N_v^{1d}
_a	2π	128	0.5	2.0	0.05000	40	2.26	1.388	0.035355	88
_b	2π	256	0.5	2.0	0.02500	80	2.26	1.388	0.017678	177
_c	2π	512	0.5	2.0	0.01250	160	2.26	1.388	0.008839	355
_d	2π	1024	0.5	2.0	0.00625	320	2.26	1.388	0.004419	710

Table 2
Runs for the TG-QT case. Parameters used in the GP solver (cases TG_a to TG_d) and the imaginary-time (IT) ARGLE solver (cases TG_aIT to TG_dIT). For each space resolution N_x, the corresponding physical and numerical parameters are displayed in Table 1.

Run	N_x	δt	T_f	Run	N_x	$[\gamma_d/4]$	$\delta\tau$	τ_f
TG_a	128	1.250e−3	12	TG_aIT	128	3	1.2500e−2	60
TG_b	256	6.250e−4	12	TG_bIT	256	6	6.2500e−3	60
TG_c	512	3.125e−4	12	TG_cIT	512	12	3.1250e−3	60
TG_d	1024	3.125e−4	10	TG_dIT	1024	25	1.5625e−3	60

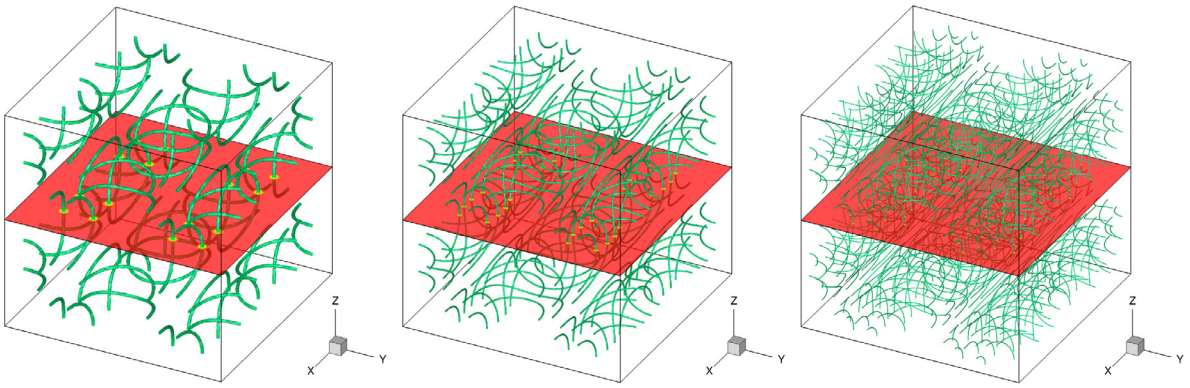

Fig. 4. TG-QT. Initial condition computed with the imaginary-time ARGLE solver. Vortex lines (iso-surfaces of low ρ) of the converged wave function ϕ_{TG} at final imaginary-time τ_f. From left to right: grid resolutions $N_x = 128$, 256, 512 (corresponding to runs TG_aIT, TG_bIT and TG_cIT in Table 2).

were considered for some cases. For all simulations, the grid is equidistant in each space direction, covering a domain of the same size $[0, \mathcal{L}]^3$, with $\mathcal{L} = 2\pi$. We recall that a Fourier spectral spatial discretization with periodic boundary conditions is used in the GP solvers.

Using the contribution by Nore et al. [34] as guideline, the reference Mach number was fixed to $M_{\text{ref}} = 0.5$, equivalent to a non-dimensional speed of sound $c = 2$. Consequently, $\alpha\beta = 2$ for all cases.

Following (53), when increasing the grid resolution N_x by a factor of 2, the value of the parameter α is diminished by the same factor in order to keep constant the value of $k_{max}\xi = 8\sqrt{2}/5 = 2.26$. There are two main consequences of this setting: the non-dimensional value of the healing length $\xi = \sqrt{2}\alpha M_{\text{ref}}$ diminishes when N_x is increased, while the grid resolution of a vortex is kept constant $\delta x/\xi = \pi/(k_{max}\xi) = 1.388$. We check for the TG case that this grid resolution is enough to accurately resolve vortices in our QT simulations. Since the size $\mathcal{L}$ of the computational box is kept constant, the higher the grid resolution N_x, the larger is the number of vortices present in the domain (see values of N_v^{1d} in Table 1).

7.1. Benchmark #1: Taylor–Green quantum turbulence (TG-QT)

The Taylor–Green initial field was prepared as described in Section 6.1. We display in Table 2 the values of the time step δt used in the GP solver (see Section 5.3) and the final time T_f of each simulation. The parameters of the corresponding imaginary-time (IT) run cases preparing the initial condition using the ARGLE solver are also presented, with $\delta\tau$ and τ_f the imaginary-time step and final value at convergence, respectively, and $[\gamma_d/4]$ the winding number of initial TG vortices seed at $\tau = 0$ (see Eq. (79) and Fig. 1).

7.1.1. Results for the imaginary time (ARGLE) procedure

In defining this benchmark, it is important to describe in detail the initial field obtained after the imaginary time (ARGLE) procedure. We recall that this procedure starts from the ansatz ψ_{ARGLE}(79) containing multiple zero TG vortices that split into $[\gamma_d/4] = [1/(2\pi\alpha)]$ singly quantized vortices during the imaginary time propagation (see Fig. 1 illustrating the case TG_aIT). Note from Table 2 that when increasing the grid resolution N_x, the ansatz TG vortices split in a larger number of individual quantized vortices (up to 25 for $N_x = 1024$). This is illustrated in Fig. 4 showing vortex configurations obtained at the end of the ARGLE procedure for runs TG_aIT, TG_bIT and TG_cIT.

To validate the ARGLE runs, we report in Table 3 the values of different energies (see Section 4.1) computed for the final field (at τ_f). The results are in good agreement with those reported by Nore et al. [34,44]. The values of the helicity (see Section 4.3) are also reported in Table 3. Note that in this particular case, we expect the helicity to be zero, which is satisfied for regularized helicity. As already stated by Clark di Leoni et al. [37], the regularized helicity is smoother and less noisy, which explains the discrepancies for helicity in runs TG_cIT and TG_dIT.

Table 3
TG-QT. Values of different energies and helicity at τ_f for the runs preparing the Taylor–Green initial condition, using the imaginary-time ARGLE solver.

Run	E^i_{kin}	E^c_{kin}	E_q	E_{int}	H	H_{reg}
TG_aIT	0.12901707	4.8667051e−04	7.9239425e−03	1.2995235e−02	1.37e−13	−1.87e−11
TG_bIT	0.11334487	2.2334712e−04	4.0373670e−03	6.8223665e−03	2.96e−07	−5.52e−07
TG_cIT	0.12884207	1.5065059e−04	2.4895687e−03	4.2864757e−03	3.83e−03	−5.63e−07
TG_dIT	0.12968555	9.5590716e−05	1.3476259e−03	2.3466209e−03	−3.94e−04	−9.71e−08

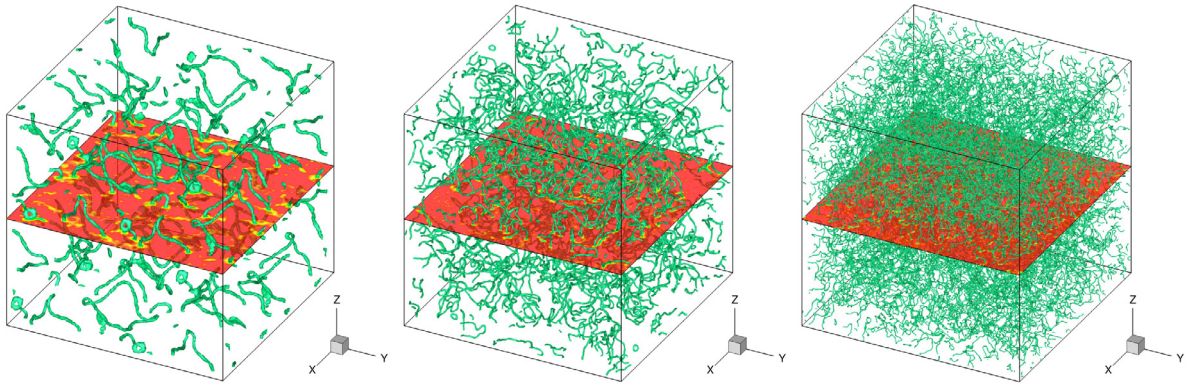

Fig. 5. TG-QT. Instantaneous fields computed with the real-time GP solver, starting from the initial condition presented in Fig. 4. Vortex lines (iso-surfaces of low ρ) of the wave function at final time T_f. From left to right: grid resolutions $N_x = 128, 256, 512$ (corresponding to runs TG_a, TG_b and TG_c in Table 2).

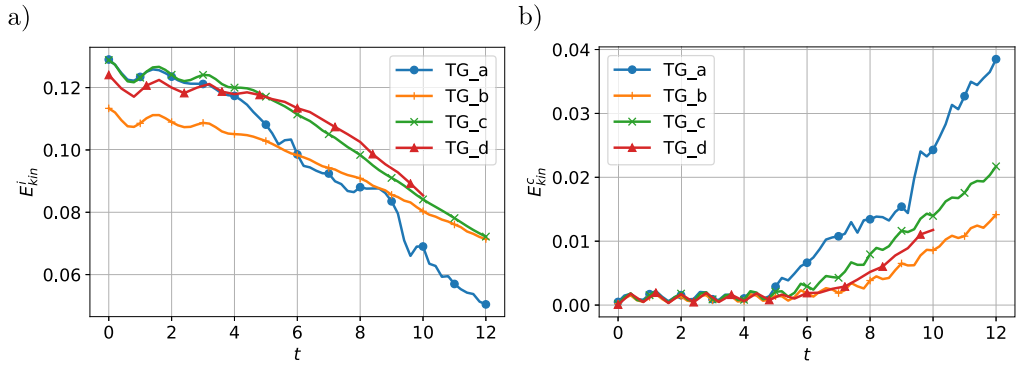

Fig. 6. TG-QT. Time evolution of incompressible kinetic energy $E^{\text{i}}_{\text{kin}}$ (a) and compressible kinetic energy $E^{\text{c}}_{\text{kin}}$ (b) for runs TG_a to TG_d (see Table 2).

7.1.2. Results for the TG-QT

Starting from the initial condition presented in Fig. 4, we used the Strang–splitting GP solver (see Section 5.3) to advance the wave function in real time. The final (at $t = T_f$) QT field is displayed in Fig. 5 for runs TG_a, TG_b and TG_c. As explained before, when the grid resolution N_x is increased, the size of a vortex core ξ diminishes and, consequently, the density of the tangled vortex lines is increased in the computational box. Meanwhile, we recall that the grid resolution of the vortex core ($\delta x/\xi$) is the same for all simulations.

To compare our results with those reported by Nore et al. [34,44], the TG-QT fields are analysed by providing in Fig. 6 the time evolution of the incompressible ($E^{\text{i}}_{\text{kin}}$) and compressible ($E^{\text{c}}_{\text{kin}}$) parts of the kinetic energy (60) for cases TG_a to TG_d. For each case, the incompressible kinetic energy is dominant at the beginning of the simulation, and slowly decreases in time, while the compressible part increases. We report in Fig. 7(a) the spectrum of $E^{\text{i}}_{\text{kin}}$ for the case TG_c at different time instants of the computation. For small k, the spectrum follows a (Kolmogorov-like) power law $E^{\text{i}}_{\text{kin}}(k) \sim k^{-5/3}$ (dashed line in Fig. 7 a), especially for early times of the simulation. These results concerning the incompressible energy evolution and its spectrum are in very good agreement with the numerical results reported by Nore et al. [34,44] for the grid resolution $N_x = 512$. As a novel diagnostic tool of the turbulent field (not presented in Nore et al. [34,44]), we show in Fig. 7(b) the time-evolution of the second-order structure function $S^2_{/\!/}(r)$ (see Eq. (37)). For a developed QT field at $t = 12$, the slope of the structure function curve at the origin is close to 2, while for large length scales the slope evolves towards 2/3. Using Eq. (38) to check the structure function calculation, we also plot in Fig. 7(b) as a dotted line the value $2\int v_x^2\, d\mathbf{x}$ which is reached for large length scales (see Eq. (38)).

7.1.3. Accuracy of numerical results

There are two important check-points in validating a QT-GP simulation: the accuracy in verifying conservation laws (see Section 2) and the grid convergence. In our numerical simulations, we monitor the time variation of the number of particles N (see Eq. (54)) and total energy per volume unit E (see Eq. (55)). These two quantities should be conserved by the GP solver. For the TG-QT simulations,

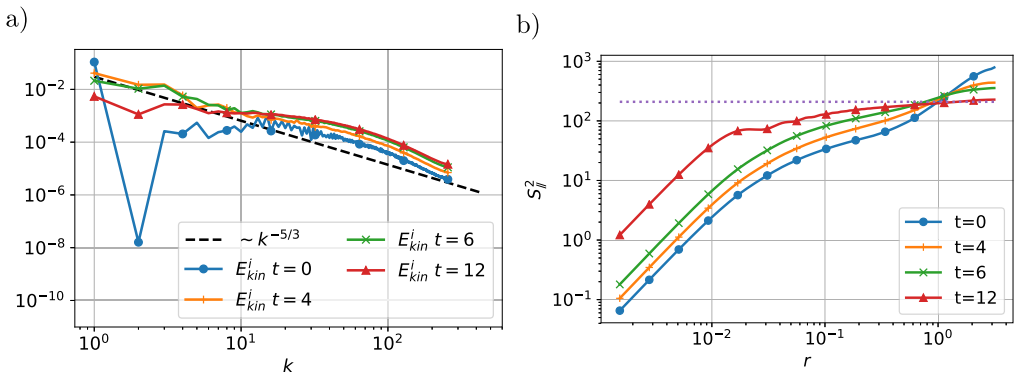

Fig. 7. TG QT. Spectrum of E^i_{kin} (a) and second-order structure function (b) for the case TG_c (see Table 2).

Table 4
TG-QT. Conservation of the number of particles N and energy per volume unit. Initial (at $t = 0$) and final values (and $t = T_f$) and relative maximum variation, defined following *e.g.* $\delta(E) = \max_{t\in[0;T_f]} |E(t) - E_{t=0}| / E_{t=0}$.

Run	$N_{\|t=0}$	$N_{\|t=T_f}$	$\delta(N)$	$E_{\|t=0}$	$E_{\|t=T_f}$	$\delta(E)$
TG_a	0.9789997	0.9789997	0.0	0.1504230	0.1504111	7.97e−05
TG_b	0.9873160	0.9873160	0.0	0.1244280	0.1244235	3.60e−05
TG_c	0.9920083	0.9920083	0.0	0.1357688	0.1357597	6.67e−05
TG_d	0.9955732	0.9955732	0.0	0.1275738	0.1275550	1.47e−04

Table 5
TG-QT. Supplementary runs used to check the grid convergence of the results (to be compared to runs in Table 1).

Run	N_x	α	β	$\xi k_{\max}$	$\delta x/\xi$
TG_a	128	0.05	40	2.26	1.388
TG_g	64	0.05	40	1.13	2.776
TG_h	256	0.05	40	4.52	0.694

Table 6
TG-QT. Energies computed from ϕ_{TG}, the wave function obtained at the end of the imaginary-time ARGLE procedure for cases TG_a, TG_g and TG_h. Relative errors (rel. err.) were computed with respect to reference values of the case TG_a.

	TG_a	TG_g	(rel. err.)	TG_h	(rel. err.)
E^i_{kin}	1.29017e−01	1.29896e−01	(6.82e−03)	1.29562e−01	(4.23e−03)
E^c_{kin}	4.86671e−04	1.24066e−03	(1.55e+00)	2.72478e−04	(4.40e−01)
E_q	7.92394e−03	1.08017e−02	(3.63e−01)	7.80383e−03	(1.52e−02)
E_{int}	1.29952e−02	9.94301e−03	(2.35e−01)	1.30274e−02	(2.48e−03)
E_v	7.10060e−01	6.98672e−01	(1.60e−02)	7.10095e−01	(4.98e−05)

we report in Table 4 initial and final values for the norm and normalized energy, as well as their relative maximum variation during the time evolution. Note from Table 4 that N is perfectly conserved, and energy relative fluctuations $\delta(E)$ are less than 0.02%, which is sufficiently small value to guarantee the validity of the computation.

The second important check-point is the grid convergence. To correctly capture vortices of radius ξ, we need enough discretization points in each vortex core. We recall that the grid step size was fixed to $\delta x/\xi = 1.338$ for all runs, corresponding to $\xi k_{\max} = \frac{8\sqrt{2}}{5} \simeq 2.26$ (see Table 1). To check the influence of this parameter on the accuracy of the QT simulation, we performed two other runs reported in Table 5, with double (TG_g) or half (TG_h) grid step size $\delta x/\xi$.

In Table 6, we report the values of different energies obtained at the end of the imaginary-time ARGLE procedure for these new cases. Relative errors were computed with respect to reference values of the case TG_a. We conclude that a value of $\xi k_{\max} \simeq 2$, *i.e.* $\delta x/\xi = \pi/2$, is sufficient to ensure the grid convergence and good accuracy of numerical results. To further check this assessment, we also simulated the QT evolution starting from these runs. We report in Fig. 8 the time evolution of incompressible and compressible kinetic energies. The similarities between cases TG_a and TG_h suggest that the resolution used for the case TG_a is fine enough to capture the vortices in the QT field. This validates the choice of parameters in Table 1.

7.2. Benchmark #2: Arnold–Beltrami–Childress quantum turbulence (ABC-QT)

The ABC initial field was prepared as described in Section 6.2. We display in Table 7 the values of the time step δt used in the GP solver (see Section 5.3) and the final time T_f of each simulation. The parameters of the corresponding imaginary-time (IT) run cases preparing the initial condition using the ARGLE solver are also presented, with $\delta\tau$ and τ_f the imaginary-time step and final value at convergence, respectively.

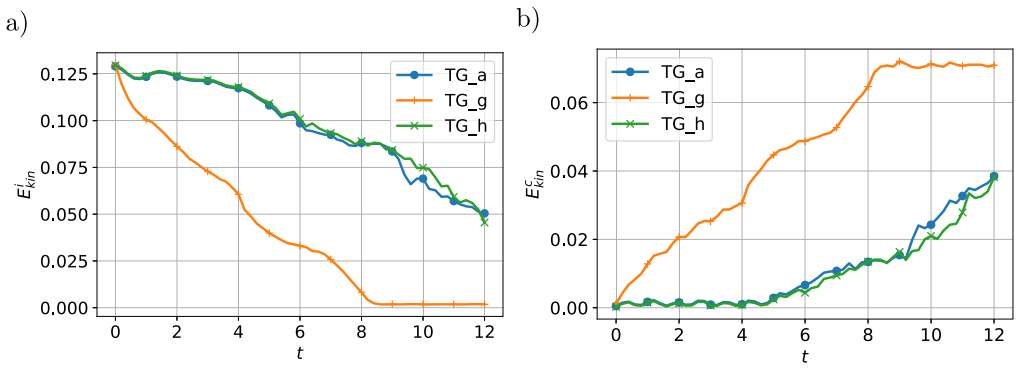

Fig. 8. TG-QT. Time evolution of incompressible $E^{\mathrm{i}}_{\mathrm{kin}}$ (a) and compressible $E^{\mathrm{c}}_{\mathrm{kin}}$ (b) energies for cases TG_a, TG_g, TG_h, used to check grid convergence.

Table 7
Runs for the ABC-QT case. Parameters used in the GP solver (cases ABC_a to ABC_c) and the imaginary-time (IT) ARGLE solver (cases ABC_aIT to ABC_cIT). For each space resolution N_x, the corresponding physical and numerical parameters are displayed in Table 1.

Run	N_x	δt	T_f	Run	N_x	$\delta\tau$	τ_f
ABC_a	128	8.0e−4	10	ABC_aIT	128	4.0e−3	30
ABC_b	256	4.0e−4	10	ABC_bIT	256	2.0e−3	30
ABC_c	512	2.0e−4	10	ABC_cIT	512	1.0e−3	30

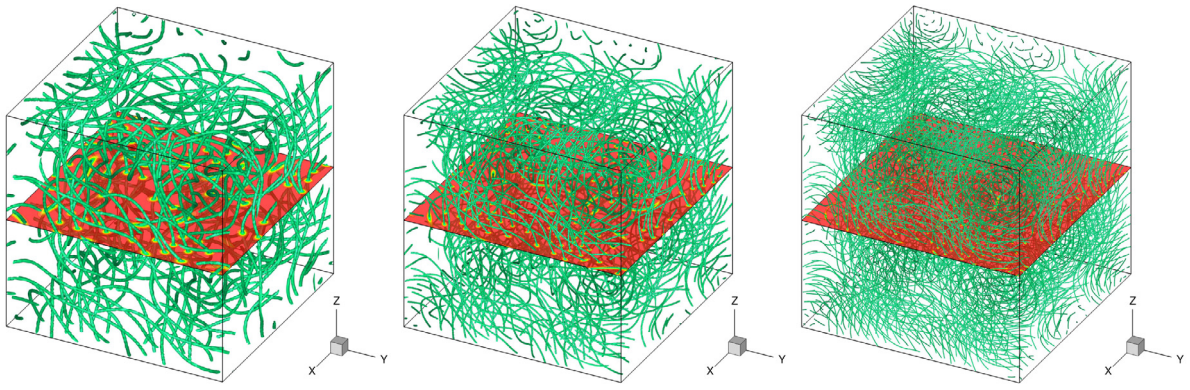

Fig. 9. ABC-QT. Initial condition computed with the imaginary-time ARGLE solver. Vortex lines (iso-surfaces of low ρ) of the converged wave function ϕ_{ABC} at final imaginary-time τ_f. From left to right: grid resolutions $N_x = 128, 256, 512$ (corresponding to runs ABC_aIT, ABC_bIT and ABC_cIT in Table 7).

7.2.1. Results for the imaginary time (ARGLE) procedure

Following (82) and (83), the initial condition for the imaginary-time ARGLE procedure is obtained only by phase manipulations of the wave function. Therefore, vortices are not present at $\tau = 0$, but they nucleate during the imaginary-time evolution, which a dissipative process. The obtained fields with vortices at the end of the ARGLE procedure are illustrated in Fig. 9. Note that, compared to the TG fields in Fig. 4, the distribution of vortices in the computational box displays no symmetries with respect to central planes. This is the first feature that makes the ABC case different from the TG case.

The second differentiating feature is the presence of helicity in the ABC flow obtained after the ARGLE procedure. We recall that the helicity of the TG flow is strictly zero (see Table 3). We report in Table 8 the values of different energies (see Section 4.1) and helicity computed for the final ABC field (at τ_f). As expected, the value of the incompressible kinetic energy is close to 1, which corresponds to the energy of the classical ABC flow. For the helicity, the theoretical value for the classical ABC flow is 3. A close value to 3 is obtained only for large grid resolutions ($N_x \geq 256$), *i.e.* for sufficiently small values of the vortex size ξ.

For these computations, the ARGLE procedure required a significant computational time and was therefore stopped before the convergence criterion (65) was satisfied. The complex inhomogeneous topological structure of the ABC flow and the large number of vortices in the flow slowed-down the convergence of the imaginary-time ARGLE procedure. We observed that the energy could be further slightly diminished, but the resulting final stationary state displayed only slight changes in the position of the peripheral vortices in the computational box. To ensure the validity of the ARGLE solution, we estimated the criterion (66) by monitoring in Fig. 10a the imaginary-time evolution of energy fluctuations defined as $|E_{\mathbf{v}}(\phi^{n+1}) - E_{\mathbf{v}}(\phi^n)|/(\delta\tau E_{\mathbf{v}}(\phi^n))$, with $E_{\mathbf{v}}$ expressed by (61). The convergence criterion (66) is satisfied to a fairly good degree of precision (10^{-3}). Figure 10b shows the spectra of $E^{\mathrm{i}}_{\mathrm{kin}}$, the incompressible kinetic energy of ARGLE solutions. This is an important benchmark verification, since $E^{\mathrm{i}}_{\mathrm{kin}}$ represents the most important part in the total energy of the ABC super-flow (see Table 8). The similar slopes of the spectra for large wave numbers k indicate that the energy distribution of the three ABC flows are similar at small scales. The low-k part of the spectrum ($k \ll k_\xi$) reproduces the classical spectrum which has only 2 nonzero modes, $k = 1, 2$. The slope for $k \gg k_\xi$ is -3 (*i.e.* $E^{\mathrm{i}}_{\mathrm{kin}}(k) \sim k^{-3}$). This feature of the high-k spectrum is detailed in [47].

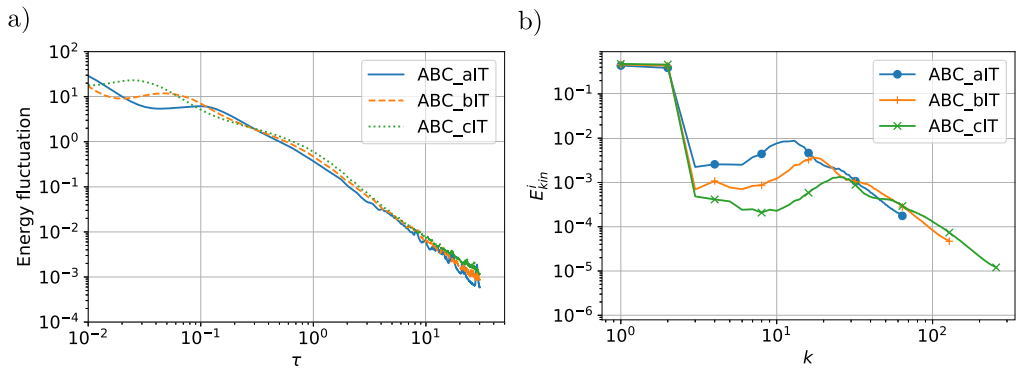

Fig. 10. ABC-QT. (a) Relative fluctuation of the total energy ($|E_{\mathbf{v}}(\phi^{n+1}) - E_{\mathbf{v}}(\phi^n)|/(\delta\tau E_{\mathbf{v}}(\phi^n))$) during the ARGLE computation. (b) Spectrum of $E^{\mathrm{i}}_{\mathrm{kin}}$, the incompressible kinetic energy of ARGLE solutions. Results for cases ABC_aIT, ABC_bIT and ABC_cIT described in Table 7.

Table 8
ABC-QT. Values of different energies and helicity at τ_f for the runs preparing the ABC initial condition, using the imaginary-time ARGLE solver.

Run	E^i_{kin}	E^c_{kin}	E_q	E_{int}	H	H_{reg}
ABC_aIT	0.9485114	0.0014218	0.0277287	0.0430379	2.4106982	2.4726091
ABC_bIT	0.9792042	0.0008142	0.0144931	0.0237201	2.7439625	2.6532860
ABC_cIT	0.9884992	0.0006486	0.0073802	0.0124975	2.7217161	2.7365301

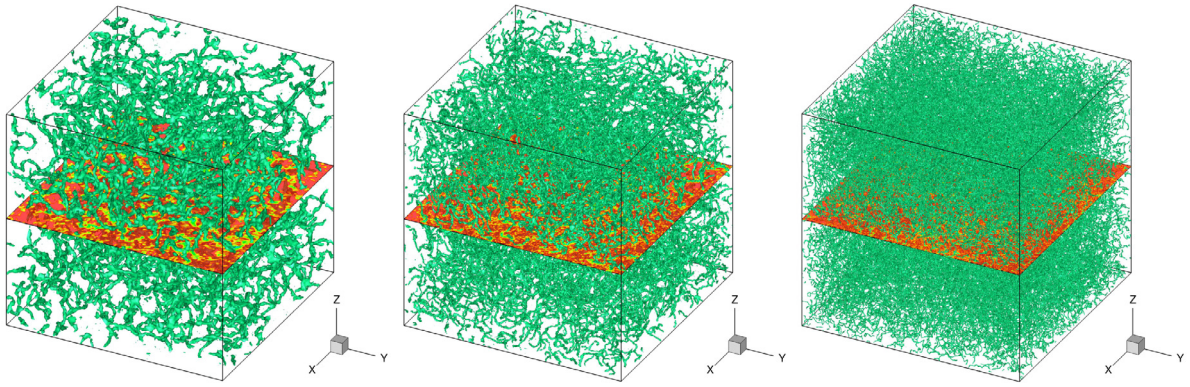

Fig. 11. ABC-QT. Instantaneous fields computed with the real-time GP solver, starting from the initial condition presented in Fig. 9. Vortex lines (iso-surfaces of low ρ) of the wave function at final time T_f. From left to right: grid resolutions $N_x = 128, 256, 512$ (corresponding to runs ABC_a, ABC_b and ABC_c in Table 7).

7.2.2. Results for the ABC-QT

Starting from the initial condition presented in Fig. 9, we used the Strang–splitting GP solver (see Section 5.3) to advance the wave function in real time. The final (at $t = T_f$) QT field is displayed in Fig. 11 for runs ABC_a, ABC_b and ABC_c. As for the TG case, when the grid resolution N_x is increased, the size of a vortex core ξ diminishes and, consequently, the density of the tangled vortex lines is increased.

The time evolution of the incompressible kinetic energy $E^{\mathrm{i}}_{\mathrm{kin}}$ and the regularized helicity H_{reg} (see Eq. (43)) are shown in Fig. 12. These results are in good agreement with those reported by Clark di Leoni et al. [37].

To analyse the turbulent super-flow, we plot in Fig. 13 spectra for the incompressible kinetic energy $E^{\mathrm{i}}_{\mathrm{kin}}$ (panel a) and the regularized helicity H_{reg} (panel b) at different time instants and the second-order structure function $S^2_{/\!/}(r)$ (panel c). We plot with dashed lines in Figs. 13a and 13b the reference (Kolmogorov-like) power laws $\varepsilon^{2/3}k^{-5/3}$ for $E^{\mathrm{i}}_{\mathrm{kin}}$ and $\eta\varepsilon^{-1/3}k^{-5/3}$ for helicity, respectively. The constants ε and η were computed as:

$$\varepsilon = -\left.\frac{dE^{\mathrm{i}}_{\mathrm{kin}}}{dt}\right|_{t=10}, \qquad \eta = -\left.\frac{dH}{dt}\right|_{t=10}. \tag{100}$$

We note from Figs. 13a and 13b that for $t > 5$, both energy and helicity H_{reg} spectra exhibit at large scales a power law variation with exponent $-5/3$, compatible with a dual energy and helicity cascade. Again, this result is in good agreement with the results of Clark di Leoni et al. [37]. The novel diagnostic tool introduced in the previous section for the TG flow is also performed with the ABC flow by computing the second-order structure function $S^2_{/\!/}(r)$ (see Eq. (37)). Figure 13c displays the structure function for the same case ABC_c and same time instants considered for plotting spectra. A similar evolution as noted for the TG case (see Fig. 7) is observed: the slope of the structure function curve at the origin is close to 2, and, for large length scales, the asymptotic value $2\int v_x^2\, d\mathbf{x}$ (dotted line) is reached.

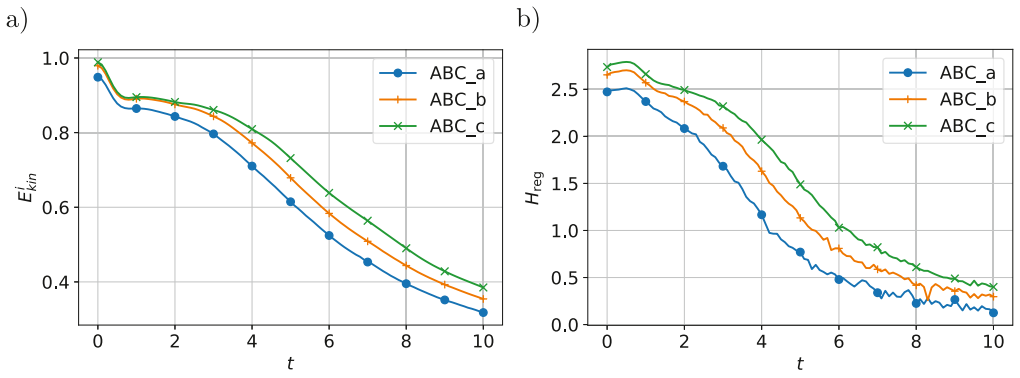

Fig. 12. ABC-QT. Time evolution of incompressible kinetic energy $E^{\mathrm{i}}_{\mathrm{kin}}$ (a) and regularized helicity H_{reg} (b) (see Eq. (43)).

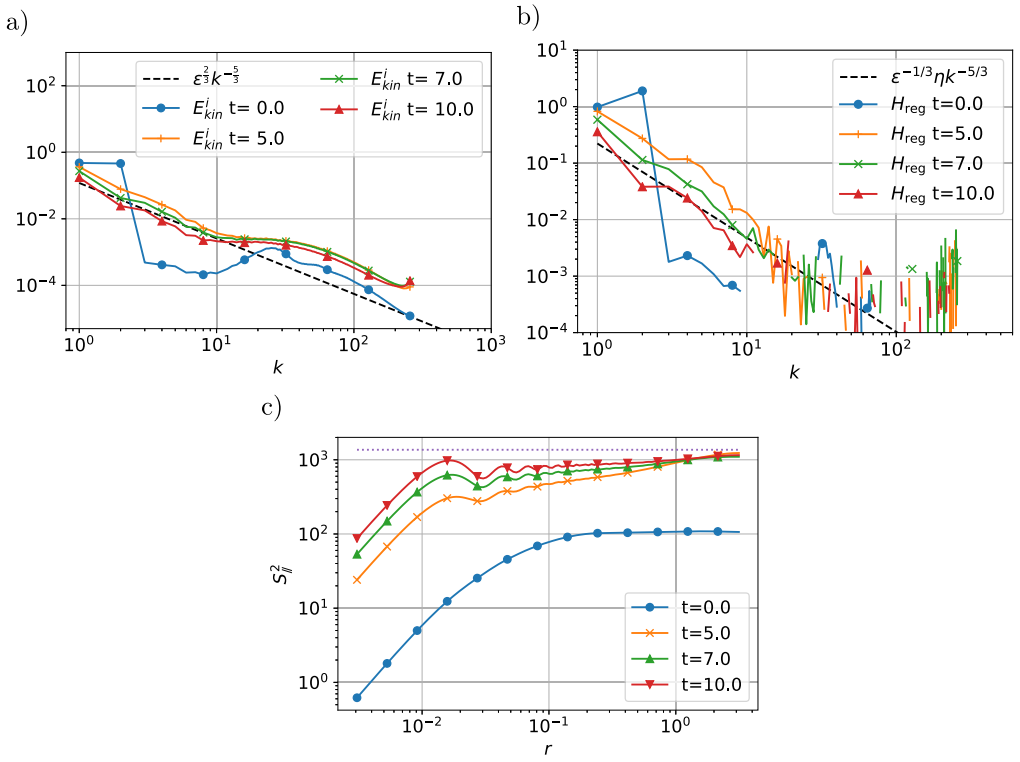

Fig. 13. ABC-QT. Analysis of the turbulent super-flow. Spectrum of incompressible kinetic energy $E^{\mathrm{i}}_{\mathrm{kin}}$ (a) and regularized helicity H_{reg} (b) at different time instants for case ABC_c. Dashed lines represent reference power laws with slope $-5/3$. Panel (c) displays the second order structure function for the same case ABC_c and same time instants.

Table 9
ABC-QT. Conservation of the number of particles N and energy per volume unit. Initial (at $t = 0$) and final values (and $t = T_f$) and relative maximum variation, defined following *e.g.* $\delta(E) = \max_{t\in[0;T_f]} |E(t) - E_{t=0}| / E_{t=0}$.

Run	$N_{\|t=0}$	$N_{\|t=T_f}$	$\delta(N)$	$E_{\|t=0}$	$E_{\|t=T_f}$	δE
ABC_a	0.9410138	0.9410138	0.0	1.0206996	1.0206400	5.98e−05
ABC_b	0.9647786	0.9647786	0.0	1.0182316	1.0181689	6.18e−05
ABC_c	0.9796053	0.9796053	0.0	1.0090255	1.0089631	6.19e−05

7.2.3. Accuracy of numerical results and influence of the Mach number

As for the TG case, we monitor the time variation of the number of particles N (see Eq. (54)) and total energy per volume unit E (see Eq. (55)). The accuracy to which these two quantities are conserved by the GP solver is reported in Table 9 initial and final values for the norm and normalized energy, as well as their relative maximum variation during the time evolution. Note from Table 4 that N is perfectly conserved, and energy relative fluctuations $\delta(E)$ are less than 0.01%, which is sufficiently small value to guarantee the validity of the computation.

Another interesting question that can be addressed using the ABC flow is the influence of the Mach number on the QT dynamics. Since the velocity $\mathbf{v}$ is singular at the vortex centre $r = 0$, we considered in defining the local Mach number the quantity $\sqrt{\rho}\mathbf{v}$ which

Table 10
ABC-QT. Runs used to test of the influence of the Mach number. Compared to run ABC_c (see Table 7), only the constants A, B, C in defining the ABC flow were modified (see Eq. (83)).

Name	(A, B, C)	N_x	$\mathcal{M}_{\max}$	$\mathcal{M}_{rms}$
ABC_c	$(0.9, 1, 1.1)/\sqrt{3}$	512	1.486860	0.703259
ABC_c1	$(0.9, 1, 1.1)/(2\sqrt{3})$	512	0.836509	0.357021
ABC_c2	$2(0.9, 1, 1.1)/\sqrt{3}$	512	2.800959	1.385344

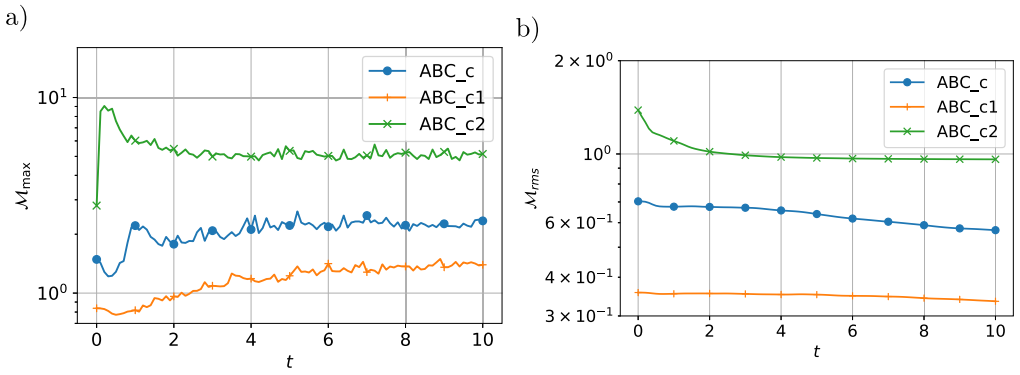

Fig. 14. ABC-QT. Time evolution of the Mach number $\mathcal{M}_{\max}$ (a) and $\mathcal{M}_{rms}$ (a) for cases ABC_c, ABC_c1 and ABC_c2 (see Table 10).

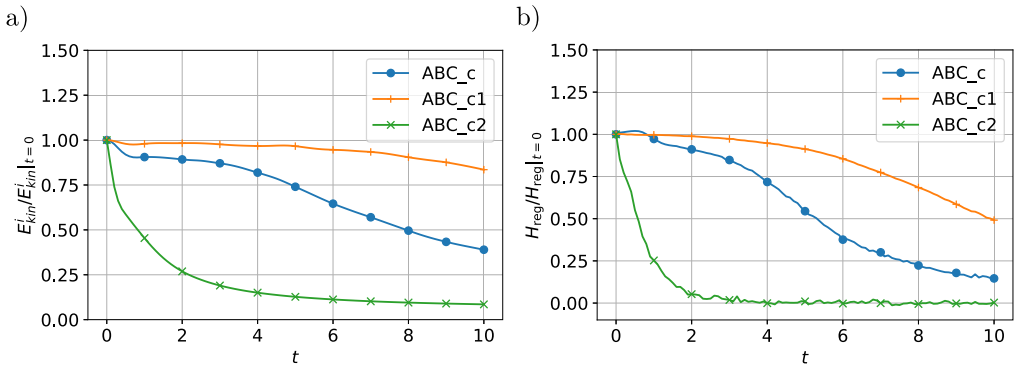

Fig. 15. ABC-QT. Influence of the Mach number. Time evolution of the incompressible kinetic energy $E^{\mathrm{i}}_{\mathrm{kin}}$ (a) and regularized helicity H_{reg} (b). To be compared with curves in Fig. 12.

is not singular ($\mathbf{v} \sim 1/r$ and $\sqrt{\rho} \sim r$, see Section 3.2). We thus computed two representative values: a maximum Mach number $\mathcal{M}_{\max}$ based on the maximum superfluid velocity, and a Mach number $\mathcal{M}_{rms}$ based on averaged values:

$$\mathcal{M}_{\max} := \frac{\|\sqrt{\rho}\mathbf{v}\|_{L^\infty(D)}}{c}, \qquad \mathcal{M}_{rms} := \frac{\|\sqrt{\rho}\mathbf{v}\|_{L^2(D)}}{c\sqrt{\mathcal{L}^3}} = \frac{\sqrt{2E_{\mathrm{kin}}}}{c}. \tag{101}$$

Keeping c and ξ constant, one can change the Mach number in the ABC flow by tuning the values of the parameters A, B, C in (83). Using as reference the case ABC_c ($N_x = 512$) we performed two new runs for which the parameters are displayed in Table 10. The values of constants A, B, C were divided (ABC_c1) or multiplied (ABC_c2) by a factor of 2. As a result, compared to case ABC_c, the velocities are divided (resp. multiplied) by 2 for case ABC_c1 (resp. ABC_c2). The values for the Mach number reported in Table 10 were computed at the end of the ARGLE procedure preparing the initial condition. Figure 14 shows the time evolution for the two values of the Mach number, $\mathcal{M}_{\max}$ and $\mathcal{M}_{rms}$ computed by the (real-time) GP solver. The ratio of 2 is well conserved in time, though the values are varying significantly. This proves that tuning the values of constants A, B, C is a simple and practical approach in modifying the Mach number of the QT super-flow.

We present in Fig. 15 the time evolution of incompressible kinetic energy $E^{\mathrm{i}}_{\mathrm{kin}}$ and regularized helicity H_{reg} for new cases with different Mach numbers. As expected from the analysis above, the energy and helicity associated with the classical flow $\mathbf{v}_{ABC}$ are divided (resp. multiplied) by 4 for case ABC_c1 (resp. ABC_c2). We note that the time evolution of these main quantities depends on the Mach number. To assess on the distribution of the incompressible kinetic energy among scales, we plotted in Fig. 16 spectra of $E^{\mathrm{i}}_{\mathrm{kin}}$ at significant time instants, $t = 5$ and final time $t = T_f = 10$. The spectra for the three cases are quite similar showing that the obtained dynamics of the QT is equivalent when varying the Mach number of the flow.

7.3. Benchmark #3: Smoothed random phase quantum turbulence (SRP-QT)

The SRP initial field was prepared as described in Section 6.3. The advantage of this new initial condition is that the time-imaginary ARGLE simulation is no longer necessary in the preparation of the initial field. We display in Table 11 the values of the time step δt

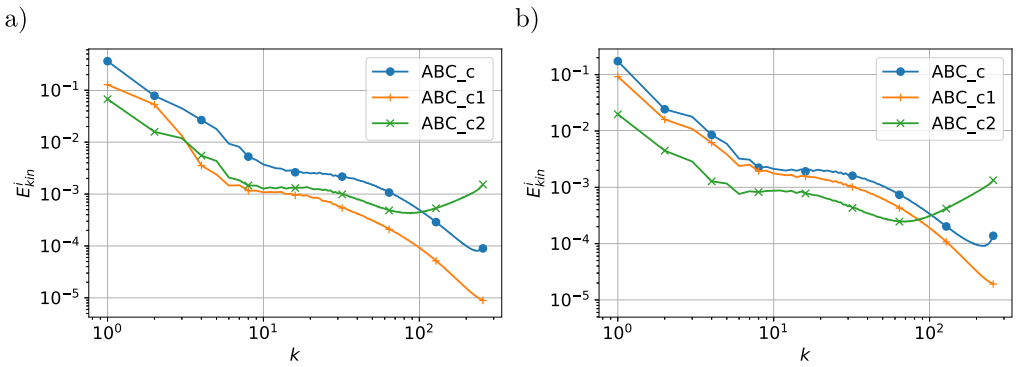

Fig. 16. ABC-QT. Influence of the Mach number. Spectrum of the incompressible kinetic energy E^i_{kin} for case ABC_c, ABC_c1, ABC_c2, at time instants $t = 5$ (a) and $t = T_f = 10$ (b).

Table 11
Runs for the SRP-QT case. For each space resolution N_x, the corresponding physical and numerical parameters are displayed in Table 1.

Run	N_x	δt	T_f	K	N_r
SRP_a	128	1/1024	8	8π	4
SRP_b	256	1/2048	8	16π	4
SRP_c	512	1/4096	8	32π	4

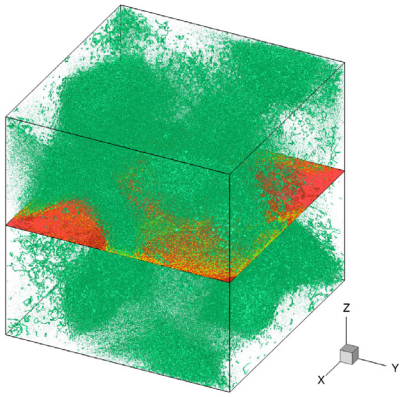

Fig. 17. SRP-QT. Instantaneous fields computed with the real-time GP solver, starting from the initial condition presented in Fig. 2. Vortex structures (iso-surfaces of low ρ) of the wave function at final time T_f. Grid resolution $N_x = 512$, corresponding to run SRP_c in Table 11).

used in the GP solver (see Section 5.3), the final time T_f of each simulation, and the parameters K (maximum amplitude of the phase) and N_r (number of random values) of the method generating the phase field (see Fig. 2). We recall that the characteristic velocity of the generated flow field results is $v = 2\alpha(KN_r/\pi)$, and the corresponding theoretical Mach number $M = \sqrt{2\alpha}KN_r/\pi\sqrt{\beta}$.

Figure 17 illustrates the vortex structures in the QT super-flow generated with this method. Compared to TG and ABC cases, in the SRP case vortices nucleate progressively and do not display long vortex lines. A very fine grain structure of vortices is observed in all SRP runs.

To analyse the SRP-QT flow we plotted in Fig. 18a the time evolution of the compressible E^c_{kin} and incompressible E^i_{kin} kinetic energies. An ensemble average for 10 different (random) initial conditions was taken to display the results. Since the initial field (at $t = 0$) does not contain vortices, the incompressible kinetic energy E^i_{kin} is initially zero and subsequently increases due to vortex nucleations. After reaching the maximum value at $t \sim 0.5$, E^i_{kin} gradually decreases to the end of the simulation ($t = T_f$). During the entire time evolution, the dynamics of the flow is dominated by the compressible kinetic energy E^c_{kin}, which is always larger than E^i_{kin}. Figure 18b shows the spectrum of E^i_{kin}. As for TG and ABC cases, a Kolmogorov-like scaling is obtained, with a $-5/3$ power-law at low wave numbers k. Hereof, the SRP-QT flow is statistically similar to the TG and ABC QT flows and can be used in a detailed parametric study of the decay of quantum turbulence (which is beyond the scope of this contribution).

7.4. Benchmark #4: Random vortex rings quantum turbulence (RVR-QT)

The RVR initial field was prepared as described in Section 6.4. Like in the SRP case, building this new initial condition avoids the use of the time-imaginary ARGLE computation. We display in Table 12 the values of the time step δt used in the GP solver (see Section 5.3), the final time T_f of each simulation, the parameter N_V representing the number of pairs of vortex rings seeded in the initial field, the radius R of a vortex ring, and the distance d between the vortex rings forming a pair (see Eq. (99)).

Note that in Fig. 3 we represented, to illustrate the method, a few number of vortex pairs (N_V=1, 20 and 50). In the GP calculations we used a much larger value for N_V, up to 800 for the case RVR_c. The initial field for the three considered cases is displayed in Fig. 19.

Table 12
Runs for the RVR-QT case. For each space resolution N_x, the corresponding physical and numerical parameters are displayed in Table 1.

Run	N_x	δt	T_f	N_V	R	d
RVR_a	128	1/1024	8	200	$\pi/2$	π
RVR_b	256	1/2048	8	400	$\pi/2$	π
RVR_c	512	1/4096	8	800	$\pi/2$	π

Like in the TG and ABC cases, when the grid resolution N_x is increased, ξ diminishes and, consequently, thinner vortex rings are seeded in the initial field.

The obtained RVR-QT flow is illustrated in Fig. 20. Multiple vortex ring reconnections lead to a dense vortex distribution in the QT field, similar to that obtained for the ABC flow (see Fig. 11).

For the analysis of the RVR-QT flow we provide in Fig. 21a the time evolution of the compressible $E^{\mathrm{c}}_{\mathrm{kin}}$ and incompressible $E^{\mathrm{i}}_{\mathrm{kin}}$ kinetic energies for the case RVR_c. Since the initial distribution of vortex rings pairs is random in the computational box, we present the ensemble average results for 10 runs with random positions of the same number of vortex ring pairs ($N_V = 800$). In the early stages of the time evolution ($t < 1$), $E^{\mathrm{i}}_{\mathrm{kin}}$ is dominant. The compressible kinetic energy $E^{\mathrm{c}}_{\mathrm{kin}}$ starts to increase at $t \sim 1$, due to sound emissions through vortex reconnections. This evolution is opposite to that observed for the SRP-QT cases. Figure 21b shows the spectrum of $E^{\mathrm{i}}_{\mathrm{kin}}$. Like in the SRP cases (see Fig. 18), we note a Kolmogorov-like scaling of the spectrum, with a $-5/3$ power-law at intermediate wave numbers k.

8. Conclusion

We simulated in this paper quantum turbulence superfluid flows described by the Gross–Pitaevskii equation. Numerical simulations were performed using a parallel (MPI-OpenMP) code based on a pseudo-spectral spatial discretization and second order splitting for the time integration. As expected from the theoretical numerical analysis, this approach ensured an accurate capture of the dynamics of the flow, with a perfect conservation of the number of particles and a negligible drift in time of the total energy. Several configurations of QT were simulated using four different initial conditions: Taylor–Green (TG) vortices, Arnold–Beltrami–Childress (ABC) flow, smoothed random phase (SRP) fields and random vortex rings (RVR) pairs. Each of these case was described in detail by setting corresponding benchmarks that could be used to validate/calibrate new GP codes. Particular care was devoted in describing dimensionless equations, characteristic scales and optimal numerical parameters. We presented values, spectra and structure functions of main quantities of interest (energy, helicity, etc.) that are useful to describe the turbulent flow. Some general features of QT were identified, despite the

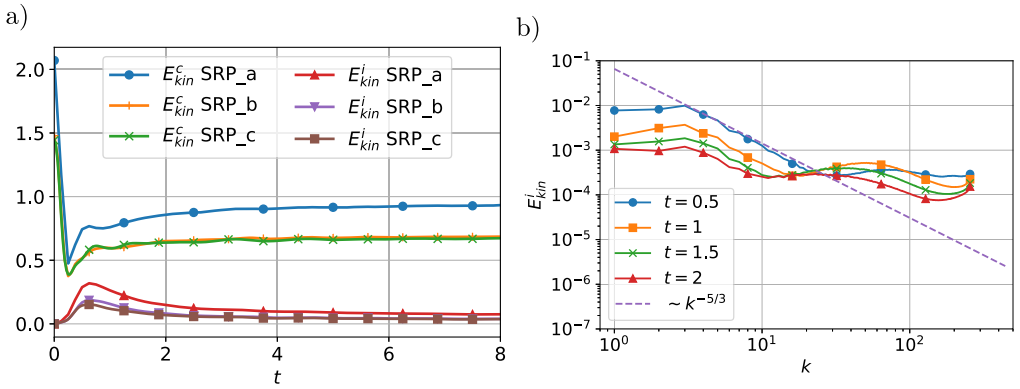

Fig. 18. SRP-QT. (a) Time evolution of the compressible $E^{\mathrm{c}}_{\mathrm{kin}}$ and incompressible $E^{\mathrm{i}}_{\mathrm{kin}}$ kinetic energies. (b) Spectrum of $E^{\mathrm{i}}_{\mathrm{kin}}$ at different time instants. Case SRP_c ($N_x = 512$). In both panels, the results represent an ensemble average for 10 different (random) initial conditions.

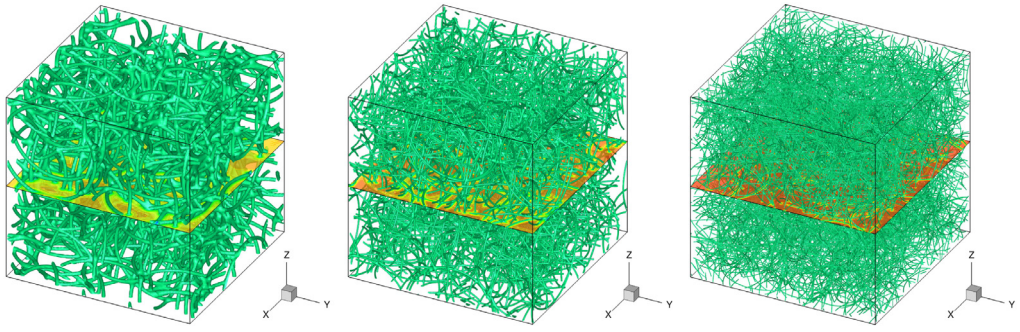

Fig. 19. RVR-QT. Initial field containing N_V randomly distributed vortex ring pairs. Vortex lines (iso-surfaces of low ρ) of the wave function. From left to right: grid resolutions $N_x = 128$, 256, 512 and $N_V = 200$, 400, 800 (corresponding to runs RVR_a, RVR_b and RVR_c in Table 12).

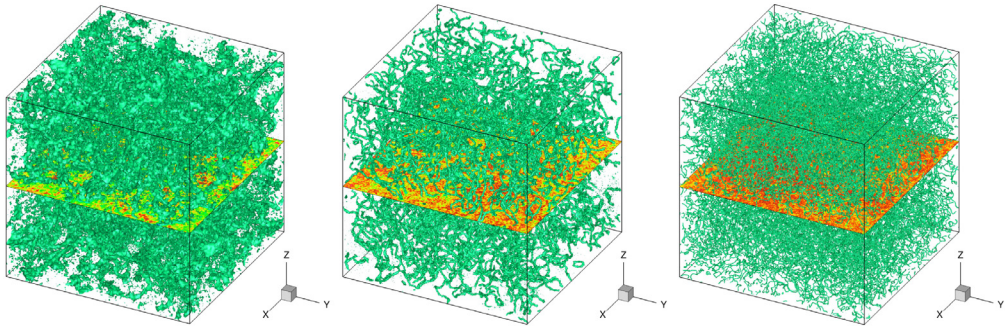

Fig. 20. RVR-QT. Instantaneous fields computed with the real-time GP solver, starting from the initial condition presented in Fig. 19. Vortex lines (iso-surfaces of low ρ) of the wave function at final time T_f. From left to right: grid resolutions $N_x = 128, 256, 512$ (corresponding to runs RVR_a, RVR_b and RVR_c in Table 12).

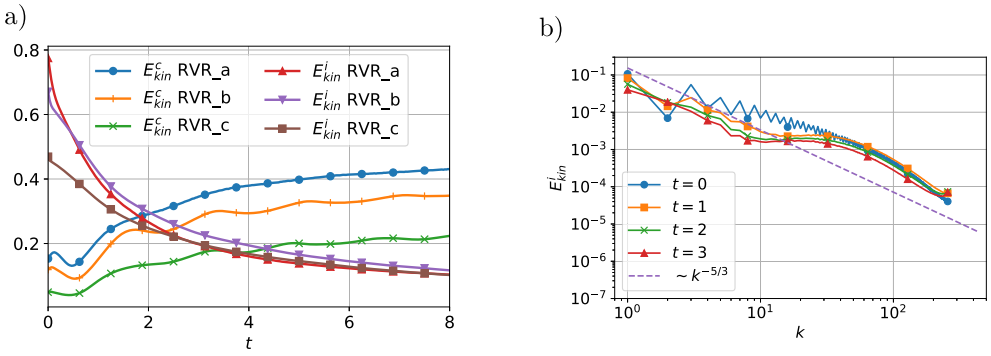

Fig. 21. RVR-QT. (a) Time evolution of the compressible E^c_{kin} and incompressible E^i_{kin} kinetic energies. (b) Spectrum of E^i_{kin} at different time instants. Case RVR_c ($N_x = 512$). In both panels, the results represent an ensemble average for 10 different runs, with random initial distribution of $N_V = 800$ vortex ring pairs in the computational domain.

variety of initial states: the spectrum of the incompressible kinetic energy exhibits a Kolmogorov-type $-5/3$ power-law scaling for the large scales, the flow dynamics is characterized by a continuous transfer between incompressible and compressible energy, etc.

The first two benchmarks (TG and ABC) are classical and inspired from classical turbulence. They start from defining a velocity field containing vortices and use an imaginary-time ARGLE procedure to reduce the acoustic emission of the initial field. The last two benchmarks (SRP and RVR) are new and based on the direct manipulation of the wave function. The new initial conditions have the advantage to be simple to implement and to avoid supplementary computations through the ARGLE procedure. The SRP initial condition has the particularity of being vortex free, with kinetic energy dominated at initial stages by its compressible part. The situation is reversed in the RVR initial condition, since at early stages the incompressible kinetic energy dominates. Therefore, the new initial conditions could be used as new QT settings to explore various physical phenomena, such as the interaction of particles with quantized vortices in QT [48]. Another possible use of the new SRP and RVR initial conditions is for the simulation of QT in atomic Bose–Einstein condensates (BEC). GP-QT dynamics in BECs is generally triggered by directly manipulating the wave function field. [49] used a randomly distributed initial wave function field, [50] applied a simple rotation of the initial field, [51] used combined rotations around two axes, while [52] suggested a random phase imprinting. The extension of our SRP and RVR models to BEC-QT will be reported in a forthcoming contribution.

Supplementary images and movies depicting the dynamics of QT-GP cases simulated in this paper are provided as Supplemental Material at http://qute-hpc.math.cnrs.fr/2020_03_QT_GP.html.

Declaration of competing interest

The authors declare that they have no known competing financial interests or personal relationships that could have appeared to influence the work reported in this paper.

Acknowledgements

The authors acknowledge financial support from the French ANR grant ANR-18-CE46-0013 QUTE-HPC. Part of this work used computational resources provided by IDRIS (Institut du développement et des ressources en informatique scientifique) and CRIANN (Centre Régional Informatique et d'Applications Numériques de Normandie).

Table A.13
Execution time for ABC runs. The last column reports the execution time divided by the number of degrees of freedom (N_x^3).

Case	N_x	Iterations	MPI proc.	Execution time (s)	Ratio
ABC_aIT	128	7500	56	539.126	0.000257075
ABC_bIT	256	15000	112	5940.076	0.000354056
ABC_cIT	512	30000	224	53066.445	0.000395375
ABC_a	128	12500	56	700.524	0.000334036
ABC_b	256	25000	112	7364.754	0.000438973
ABC_c	512	50000	224	63397.341	0.000472346

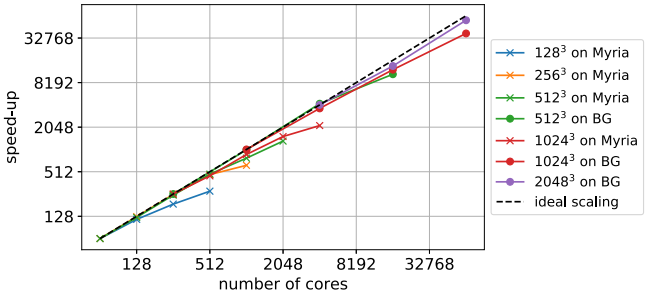

Fig. A.22. Parallel performance (speed-up) of the GPS code when computing 3D cases with 128^3, 256^3, 512^3, 1024^3 and 2048^3 grid points. Strong scalability test using only MPI (from 64 to 64,536) processes. Dashed lines represent ideal speed-up.

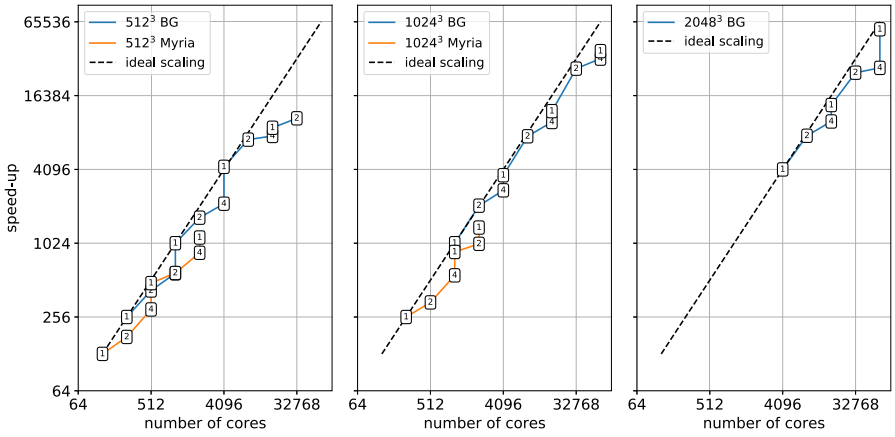

Fig. A.23. Parallel performance (speed-up) of the GPS code when computing 3D cases with 512^3, 1024^3 and 2048^3 grid points. Strong scalability test of the hybrid code MPI-OpenMP using MPI processes as in the previous test and 1, 2 or 4 OpenMP threads. Dashed lines represent ideal speed-up.

Appendix. Parallel performance of the code

A.1. Execution time

Execution times for runs ABC_a to ABC_c and ABC_aIT to ABC_cIT are reported in Table A.13. When switching from one case to the next one, we doubled the total number of iterations and also the number of processes. We expected a small variation of the value of the execution time divided by the grid resolution. For the ARGLE procedure, we monitored an efficiency of 65% from case ABC_aIT to case ABC_cIT. For the time-dependent GP simulation, we obtained an efficiency of 70% from case ABC_a to case ABC_c. Note that the measured time is the total time for the execution of the program, not solely the computational part of the code.

A.2. Strong scalability of GPS

Strong scalability results of the GPS code are presented in this section. To test the code, we used both CRIANN Myria and Idris Turing BlueGene/Q (BG) supercomputers. The supercomputer called Myria has 366 nodes, each with 28 cores (Intel Broadwell 2.4 GHz) for a total of 10,248 cores and 419 TFLOPs. The supercomputer BG has 6144 nodes, each with 16 cores (IBM PowerPC A2 1.6 GHz) for a total of 98,304 cores and 1258 PFLOPs. It must be noted that the BG supercomputer has been built to solve the bottleneck due to memory bandwidth and latency, by reducing the clock of each core. Myria has a much higher clock speed without a larger memory bandwidth and a similar interconnection between nodes. As a result, the network and memory bandwidth are playing a larger role in the performance of the code when run on Myria supercomputer than on BG. The code GPS used in this work, was first developed during the French project ANR Becasim [15] and it was tuned on the BG supercomputer to optimize its scalability. In this work, the supercomputer Myria was used in order to obtain present results. We present strong scalability results on both supercomputers. A 3D

test case (with grid resolutions up to 2048^3) was run using a different number of processes (up to 4096 for Myria, and 64,536 for BG) using the Strang second order splitting scheme and the execution time was monitored.

The first strong scalability test was performed using only MPI (Fig. A.22). It shows scalability and speed-up close to ideal performances on BG, while on Myria the speed-up is good but with a lower efficiency. The efficiency on Myria is above 75% up to 256, 512, 1024 and 2048 processes for discretizations of 128^3, 256^3, 512^3 and 1024^3, respectively. On the BG supercomputer, the efficiency is above 75% up to 4096, 16,384 and 65,536 processes for discretizations of 512^3, 1024^3 and 2048^3, respectively. The maximum acceleration measured is 2152 on Myria using 4096 processes ($N = 1024^3$) and 56,987 on BG using 65,536 processes ($N = 2048^3$).

For a further assessment of the parallel capabilities of the code, another scalability test using MPI and up to 4 OpenMP threads per MPI process was performed (Fig. A.23). Using OpenMP on the BG supercomputer resulted in an efficiency of about 80% with 4 threads. The efficiency decreases drastically with more OpenMP threads. For computations with the GPS, using OpenMP is important to decrease the cost of the input/output operations, if the run needs more than 10,000 cores. This feature could be significantly affected by the architecture of the processor available on the supercomputer. Using Myria (with no thread affinity enabled), we noticed that using more than 2 threads per process should be avoided.

References

[1] W.F. Vinen, J.J. Niemela, J. Low Temp. Phys. 128 (2002) 167–231.
[2] C.F. Barenghi, R.J. Donnelly, W.F. Vinen (Eds.), Lecture Notes in Physics, No. 571, Springer, 2001.
[3] C.F. Barenghi, Y.A. Sergeev (Eds.), CISM International Centre for Mechanical Sciences, No. 501, Springer, 2008.
[4] B. Halperin, M. Tsubota (Eds.), Progress in Low Temperature Physics, No. 16, Springer, 2009.
[5] E. Henn, J. Seman, G. Roati, K. Magalhãesw, V. Bagnato, J. Low Temp. Phys. 158 (2010) 435–442.
[6] J. Seman, E. Henn, R. Shiozaki, G. Roati, F. Poveda-Cuevas, K. Magalhães, V. Yukalov, M. Tsubota, M. Kobayashi, K. Kasamatsu, V. Bagnato, Laser Phys. Lett. 8 (2011) 691–696.
[7] J. Kwon, G. Moon, J.-y. Choi, S. Seo, Y.-i. Shin, Phys. Rev. A 90 (2014) 063627.
[8] N. Navon, A. Gaunt, R. Smith, Z. Hadzibabic, Nature 539 (72) (2016).
[9] U. Frisch (Ed.), Turbulence: The Legacy of A.N. Kolmogorov, Cambridge University Press, 1995.
[10] J. Salort, B. Chabaud, E. Lévêque, P.-E. Roche, Europhys. Lett. 97 (3) (2012) 34006.
[11] M. Tsubota, K. Fujimoto, S. Yui, J. Low Temp. Phys. 188 (2017) 119–189.
[12] M. Brachet, Comptes Rendus Physique 13 (9–10) (2012) 954–965.
[13] C. Barenghi, L. Skrbek, K. Sreenivasan, Proc. Natl. Acad. Sci. USA 111 (SUPPL. 1) (2014) 4647–4652.
[14] M. Kobayashi, M. Tsubota, J. Low Temp. Phys. 150 (3–4) (2008) 587–592.
[15] P. Parnaudeau, A. Suzuki, J.-M. Sac-Epée, 2015, GPS: An efficient & spectrally accurate code for computing Gross-Pitaevskii equation. ISC-2015, Research Posters Session, 2015, Germany.
[16] X. Antoine, R. Duboscq, Comput. Phys. Comm. 185 (11) (2014) 2969–2991.
[17] X. Antoine, C. Besse, W. Bao, Comput. Phys. Comm. 184 (12) (2013) 2621–2633.
[18] A. Minguzzi, S. Succi, F. Toschi, M.P. Tosi, P. Vignolo, Phys. Rep. 395 (2004) 223–355.
[19] W. Bao, in: P.G. Kevrekidis, D.J. Frantzeskakis, R. Carretero-González (Eds.), Transport Phenomena and Kinetic Theory: Applications To Gases, Semiconductors, Photos, and Biological Systems, Series Modeling and Simulation in Science, Engineering and Technology, Vol. 2006, Birkhauser, 2006, pp. 215–255.
[20] W. Bao, Y. Cai, Kinet. Relat. Models 6 (2013) 1–135.
[21] W. Bao, Mathematical models and numerical methods for Bose-Einstein condensation, in: Proc. of the International Congress of Mathematicians, Seoul 2014, 2014, IV, pp. 971–996.
[22] C.M. Dion, E. Cancès, Comput. Phys. Comm. 177 (2007) 787–798.
[23] M. Caliari, S. Rainer, Comput. Phys. Comm 184 (3) (2013) 812–823.
[24] X. Antoine, R. Duboscq, Comput. Phys. Comm. 193 (2015) 95–117.
[25] Z. Marojević, E. Göklü, C. Lämmerzahl, Comput. Phys. Comm. 202 (2016) 216–232.
[26] G. Vergez, I. Danaila, S. Auliac, F. Hecht, Comput. Phys. Comm. 209 (2016) 144–162.
[27] P. Muruganandam, S. Adhikari, Comput. Phys. Comm 180 (10) (2009) 1888–1912.
[28] D. Vudragović, I. Vidanović, A. Balaz, P. Muruganandam, S.K. Adhikari, Comput. Phys. Comm. 183 (9) (2012) 2021–2025.
[29] R. Caplan, Comput. Phys. Comm. 184 (4) (2013) 1250–1271.
[30] L. Kong, J. Hong, J. Zhang, Commun. Comput. Phys. 14 (1) (2014) 219–241.
[31] U. Hohenester, Comput. Phys. Comm. 185 (1) (2014) 194–216.
[32] R. Kishor Kumar, V. Lončar, P. Muruganandam, S.K. Adhikari, .A. Balaž, Comput. Phys. Comm. 240 (2019) 74–82.
[33] C. Nore, M. Brachet, S. Fauve, Physica D 65 (1–2) (1993) 154–162.
[34] C. Nore, M. Abid, M. Brachet, Phys. Fluids 9 (9) (1997) 2644–2669.
[35] M. Abid, C. Huepe, S. Metens, C. Nore, C. Pham, L. Tuckerman, M. Brachet, Fluid Dyn. Res. 33 (5–6) (2003) 509–544.
[36] P. Clark di Leoni, P. Mininni, M. Brachet, Phys. Rev. A 94 (4) (2016) 043605.
[37] P. Clark di Leoni, P.D. Mininni, M.E. Brachet, Phys. Rev. A 95 (2017) 053636.
[38] L.P. Pitaevskii, S. Stringari, Bose-EInstein Condensation, Clarendon Press, Oxford, 2003.
[39] M. Kobayashi, M. Tsubota, J. Low Temp. Phys. 148 (3–4) (2007) 275–279.
[40] R. Carles, R. Danchin, J.-C. Saut, Nonlinearity 25 (10) (2012) 2843–2873.
[41] J.C. Neu, Physica D 43 (1990) 385–406.
[42] C.F. Barenghi, N.G. Parker (Eds.), A Primer on Quantum Fluids, Springer, 2016.
[43] N. Berloff, M. Brachet, N. Proukakis, Proc. Natl. Acad. Sci. USA 111 (SUPPL. 1) (2014) 4675–4682.
[44] C. Nore, M. Abid, M. Brachet, Phys. Rev. Lett. 78 (20) (1997) 3896–3899.
[45] M. Frigo, S. Johnson, Proc. IEEE 93 (2005) 216–231.
[46] W. Bao, Q. Du, SIAM J. Sci. Comput. 25 (2004) 1674.
[47] G. Krstulovic, M. Brachet, Phys. Rev. Lett. 105 (12) (2010) 129401.
[48] U. Giuriato, G. Krstulovic, Sci. Rep. 9 (1) (2019) 4839.
[49] N. Berloff, B. Svistunov, Phys. Rev. A 66 (1) (2002) 136031–136037.
[50] N. Parker, C. Adams, Phys. Rev. Lett. 95 (14) (2005).
[51] M. Kobayashi, M. Tsubota, Phys. Rev. A 76 (4) (2007).
[52] A. White, C. Barenghi, N. Proukakis, A. Youd, D. Wacks, Phys. Rev. Lett. 104 (7) (2010).